

Perspectives on Designer Photocathodes for X-ray Free-Electron Lasers: Influencing Emission Properties with Heterostructures and Nanoengineered Electronic States


Nathan A. Moody,^{1,*} Kevin L. Jensen,² Andrew Shabaev,² Samuel G. Lambrakos,² John Smedley,³ Daniel Finkenstadt,⁴ Jeffrey M. Pietryga,¹ Petr M. Anisimov,¹ Vitaly Pavlenko,¹ Enrique R. Batista,¹ John W. Lewellen,¹ Fangze Liu,¹ Gautam Gupta,¹ Aditya Mohite,¹ Hisato Yamaguchi,¹ Mark A. Hoffbauer,¹ and István Robel¹

¹Los Alamos National Laboratory, Los Alamos, New Mexico 87545, USA

²Naval Research Laboratory, Washington, District of Columbia 20375, USA

³Brookhaven National Laboratory, Upton, New York 11973, USA

⁴United States Naval Academy, Annapolis, Maryland 21402, USA

 (Received 12 April 2017; revised manuscript received 26 May 2018; published 17 October 2018)

The development of photoemission electron sources to specifically address the competing and increasingly stringent requirements of advanced light sources such as x-ray free-electron lasers (XFELs) motivates a comprehensive material-centric approach that integrates predictive computational physics models, advanced nanosynthesis methods, and sophisticated surface-science characterization with *in situ* correlated study of photoemission performance and properties. Related efforts in material science are adopting various forms of nanostructure (such as compositionally graded stoichiometry in heterostructured architectures, and quantum features) allowing for tailored electronic structure to control and enhance optoelectronic properties. These methods influence the mechanisms of photoemission (absorption, transport, and emission) but have not, as yet, been systematically considered for use in photocathode applications. Recent results and near-term opportunities are described to exploit controlled functionality of nanomaterials for photoemission. An overview of the requirements and status is also provided.

DOI: [10.1103/PhysRevApplied.10.047002](https://doi.org/10.1103/PhysRevApplied.10.047002)

I. INTRODUCTION

Future generation x-ray light sources are considered to be the instruments of discovery science across an increasingly wide array of disciplines [1]. Extremely short, intense, coherent x-ray pulses can probe the structure and dynamics of matter on length and time scales defined by molecular resonances, electronic transitions, and the spatial scale of atomic bonds [2–4]. Grand challenges ranging from drug discovery to protein folding, and many aspects of national security, require the ability to observe and even control matter at these unprecedented scales [5]. Realizing this potential depends critically upon improvements in electron sources [6]. A design capability at the cathode is essential for obtaining the needed gain in x-ray and high-performance free-electron lasers (FELs) [7–9].

FELs (and accelerators requiring emittance-dominated beams) require, first, that the electron beam be focused inside the laser beam, and second, that the gain be maximized. The first requirement entails a severe constraint when the laser wavelength is small, as

for x-ray FELs (XFELs), and the second requirement entails that the current I be as large as possible. They are compactly addressed by demanding that brightness be high, where B is related to beam current I and emittance ε by $B \sim 2I/(\gamma\beta\varepsilon)^2$, where $\beta = v/c$ and $\gamma^2 = 1/(1 - \beta^2)$ are the usual relativistic factors. The remaining term, emittance (more often represented as normalized rms emittance $\varepsilon_{n,rms}$) governs the manner in which a beam spreads, with greater spreading as the beam propagates being identified with higher emittance. Specifically, emittance from a flat circular emission area goes as the product of the square root of the area ($\pi\rho_c^2$) of the emitting surface with the mean transverse energy (MTE) of the electrons as they are emitted, and so generally $\varepsilon_{n,rms} \propto \rho_c\sqrt{\text{MTE}}$ up to factors of order unity and constants such as mc^2 related to the electron rest energy [10]. A related concern, in particular for future XFELs, is that the electron bunches be compressed or have designed pulse shapes, and this generally demands subpicosecond rise-fall times of the bunch, translating into demands on emission promptness from the photocathodes. Low-electron-affinity semiconductors generally have the highest quantum efficiency (QE), defined

*nmood@mailaps.org

as the ratio of emitted electrons to incident photons, but this usually comes at the expense of emission promptness. This is partly due to emission of electrons that have thermalized during transport to the surface as a consequence of deep laser-penetration effects, and such thermalized tails indeed affect promptness and longitudinal emittance [11,12]. These relationships are explained in greater detail in the next section. Insofar as QE and $\varepsilon_{n,rms}$ increase with photon energy, and QE and response time both increase by exploiting otherwise fragile coated semiconductors, the various demands on the photocathodes clearly and unavoidably demand a balancing of priorities.

XFELs place demands on photocathodes that are presently unmet by existing photocathode technologies because requirements for simultaneously obtaining high QE and low emittance are correlated with bunch shape, and both QE and emittance are themselves related such that improving one compromises the other [10,13–22] because of the inversely linked physics elaborated below [23,24]. These issues remain even though aggressive and substantial efforts have been undertaken to reduce the MTE that figures prominently in the emittance figure of merit. Efforts include minimizing uncorrelated emittance growth affected by space-charge forces through beam shaping of the initial distribution [11] (thereby requiring photocathode response times smaller than a picosecond) [25], increasing the pulse length so as to enable smaller laser spot sizes [26], altering the degree of band bending at the surface of a semiconductor photocathode such as GaN so as to limit scattering effects and the randomization of momentum gain near the surface [26], and controlling the surface roughness by improving the surface preparation procedures in III-V negative-electron-affinity (NEA) photocathodes [27,28].

Using ultracold photoemitters is a means of reducing the MTE: when MTE is very low, disorder-induced heating (that is, the binary interaction of electrons in the beam) can become a significant effect [29], and investigation is underway to study how surface nonuniformity as a consequence of crystal-face variation induces MTE growth [30]. Pulse shaping, however, requires very fast (subpicosecond) response times from the photocathodes to enable both short duration and a pulse-shaping capability. Additionally, although traditional photocathode candidates have reached limits on further emittance reduction due to surface roughness [31,32] and the chemical roughness associated with work-function variation on grains, progress in controlling roughness using codeposition [33] in conjunction with stoichiometry [28] have been reported. Apart from broad modifications to the cathode in the form of doping and coatings, the engineering of photocathode properties has not, as yet, made use of recent advances in semiconductor heterostructures and nanoscale features. Paths forward discussed herein include the following:

TABLE I. Photocathode metrics: quantum efficiency, emittance, response time, lifetime, and ruggedness.

Metric	What it affects	Target goal
QE	Bunch charge yield	Large
$\varepsilon_{n,rms}$	Beam spreading	Small
Δt	Pulse shaping	Fast
Lifetime	Operational duration	Long
Ruggedness	Survivability in rf	Insensitive

(a) Control of electronic energy structure in the material by quantum-confinement methods

(b) Heterostructured surface layers that act as filters or energy selectors when photoexcited or fed by broad electron distributions [34]

(c) Stoichiometric control over optical properties, band gap and transport properties, and band bending or field penetration

(d) Improvement of surface stability through the use of protective layers

This paper provides an overview of such nanostructures and techniques, including recent results and future paths toward integration, but firstly it is crucial to understand the *impact* of photocathode metrics on the architecture and performance of XFELs.

II. PHOTOCATHODE METRICS RELEVANT FOR XFELs

Broadly, improvement is needed in each of the five photocathode performance metrics listed in Table I: (i) QE (in the form of peak and average current for a given drive laser intensity and duration), (ii) emittance $\varepsilon_{n,rms}$ (in the form of spatial spreading in the electron beam as it propagates), (iii) response time Δt , (iv) operational lifetime, and (v) ruggedness in a photoinjector environment. Simultaneous improvements in all of these parameters are needed but meeting all such goals has proven unrealistic with existing bulk photocathode materials.

The entanglement of quantum efficiency QE, emittance $\varepsilon_{n,rms}$, and response time Δt originates with the physics of electron transport through the bulk material and the barrier conditions at the surface [10,26,35]. Namely, material-dependent properties entail complex tradeoffs, most notably with respect to the band gap E_g and effective mass m_{eff} of the electron, the optical constants (n, k) that govern the laser-penetration depth $\delta(\omega)$ and the reflectivity $R(\omega)$, and the electron affinity E_a or work function Φ that are affected by both carrier concentration and the presence of volatile coatings such as cesium. Both QE and $\varepsilon_{n,rms}$ increase with photon energy [10,35], and QE increases as response time increases [25,26]. Both the deeper penetration and longer mean free paths for photoexcited electrons affect the response time of semiconductor photocathodes.

In metals, photons can excite electrons with an energy up to $\hbar\omega - \Phi$ (for Cu, $\Phi = 4.5$ eV), whereas in semiconductors up to $\hbar\omega - E_a - E_g$ (for Cs_3Sb , $E_a + E_g$ is 1.9 eV) so that the MTE can be larger, thereby increasing emittance depending on how much the photon energy exceeds the emission barrier. Accordingly, the normal (or forward) energy is also larger, which leads to increased QE (they are linked, as the total electron energy is the sum of the forward energy and MTE). And lastly, although lifetime and ruggedness appear to be distinct from QE and $\epsilon_{n,\text{rms}}$, they are not: compensating for low QE by increased drive laser power causes heat-induced damage and ion back bombardment can damage coatings in addition to the crystal lattice. Such changes affect both bulk transport and surface emission, making measured QE and $\epsilon_{n,\text{rms}}$ at a particular moment in time a consequence of the history of the photocathode while at the same time being dependent on the conditions under which the photocathode is forced to perform. Attempting to lower emittance by exciting very close to the emission threshold (i.e., limiting the excess energy of emitted electrons) is also problematic: emittance varies as $\sqrt{\hbar\omega - \phi}$ for metals and so QE falls off catastrophically when approaching the threshold (QE varies as $(\hbar\omega - \phi)^2$). These complex and interrelated tradeoffs make it very challenging to decouple the most dominant linkages between them and motivate the use of tailored or engineered electronic states.

The reconsideration of the evaluation of QE for semiconductors in the moments framework [23,24] (which shares common features with Spicer’s three-step model [10,36,37]) demonstrates the viability of the method for semiconductors, and therefore supports expectations that the same methods may also apply in the moments equations from which $\epsilon_{n,\text{rms}}$ is evaluated. Consequently, the Dowell-Schmerge relation for metals [Eq. (5) below] may require modifications for semiconductors, although the evaluation of the relation is in progress. As the analysis shows, metals and semiconductors differ through the nature of the effective electron mass, the emission probability, the existence of a band gap, and the behavior of band bending. Critically, they additionally differ in the nature of the scattering processes that affect electron transport and escape.

The scattering rate (electron-electron in metals is fast, electron-phonon in semiconductors is slower) in conjunction with the laser-penetration depth and the surface barrier all affect how fast and how long emission from photocathodes occurs [38]. Figures 1 and 2 illustrate the correlations between QE, $\epsilon_{n,\text{rms}}$, and response time. Metals have short laser-penetration depths and electron-electron ($e-e$) scattering rapidly reduces electron energy to below the work function because such collisions tend to share the energy of the colliding particles amongst the collision products. Semiconductors have deeper penetration depths but also a magic window forbidding $e-e$ scattering

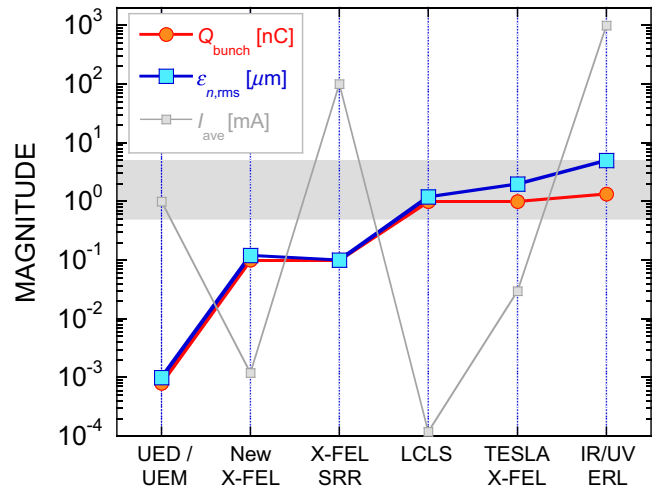


FIG. 1. Comparison of bunch charge Q_{bunch} (red line and circle), $\epsilon_{n,\text{rms}}$ (blue line and square), and average beam current I_{ave} across several classes and/or examples of existing and future electron source applications (based on discussions in Ref. [39]). Ultra-fast electron diffraction (UED) and microscopy (UEM) are time-resolved imaging techniques; these and other applications mentioned are discussed further in Ref. [39]

because no electron final states exist within the band gap. Phonon energies tend to be less than 100 meV (e.g., the Debye energy of Cu is 27 meV, of Si is 54 meV), and so electron-phonon ($e\text{-ph}$) scattering does not reduce the energy as rapidly as ($e\text{-e}$) scattering, making it less detrimental to emission. Thus, QE improves, but response time is lengthened.

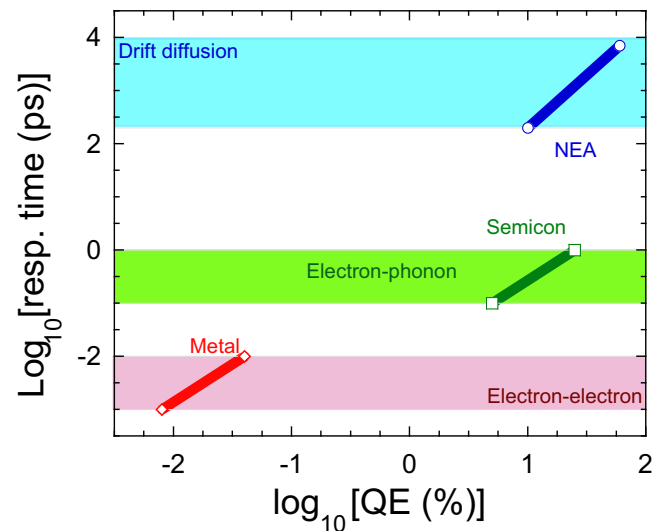


FIG. 2. QE vs response time for classes of photocathodes, based on Fig. 14 in Ref. [38]. Dominant scattering mechanisms: electron-electron (metals like Cu); electron-phonon (semiconductors like Cs_3Sb); drift diffusion (NEA like GaAs).

Lastly, a cesiated metal surface likewise improves metal photocathode QE by reducing the emission barrier [20]. In the case of semiconductors like GaAs and GaAsP, cesium termination of a surface (much like hydrogen termination of diamond) removes the barrier altogether and results in NEA surfaces, for which the vacuum level is below the conduction-band minimum. The absence of a barrier additionally has consequences for response time: thermalized electron populations generated deep in the bulk (up to a μm) can reach the surface and by virtue of NEA contribute to emitted current. Because they are drift-diffusion electrons, their contribution is in the form of long tails in the pulse that persist up to tens of picoseconds.

However, the inclusion of cesium as a surface layer negatively impacts ruggedness and lifetime [13,14,40,41]. The same mechanisms that improve transport and barrier height negatively impact response time and emittance [35]. The state of the surface, whether a polycrystalline vs single-crystal material, may also act as sources of increased emittance through geometric roughness and work-function variation [27,42,43].

Emittance is caused by several processes at various locations in relation to the surface of the cathode (termed *surface emittance*):

(a) *Intrinsic emittance* due to transverse-energy components in the emitted electron distribution itself, including changing electron effective-mass effects as the electron transits from the material into vacuum

(b) *Rough surface emittance* due to electrons being launched in directions at an angle to the beam direction caused by geometric surface structure in the form of ridges and protrusions and

(c) *Applied field emittance* due to the surface electric field at the cathode

Of these, the intrinsic emittance is often comparatively large (e.g., Fig. 23 of Ref. [44]) and its reduction is, therefore, one of the highest priorities influencing cathode design. Additionally, other sources of emittance (image charge or wakefield, space charge due to nonuniform emission, and optical aberrations and space charge) occur but do so at increasing distances (millimeters to centimeters and beyond) from the cathode surface.

Operational lifetime is another important metric for practical utilization of a photocathode in a particular electron gun. Here, we first call attention to the processes responsible for degradation and discuss how these will also affect other photocathode metrics. Although the phenomenon of photocathode QE degradation is well known [45], an understanding of the underlying processes has remained vague, as evidenced by the use of terms like poisoning [41] and routine quoting of $1/e$ lifetimes, even when the published data exhibits nonexponential QE vs time dependencies.

The view of this perspective is that as photocathodes advance, an understanding of cathode degradation and its quantitative description must likewise evolve. Ion back bombardment is the dominating mechanism of QE degradation in many cases, but its characterization is complicated because physical destruction of the cathode usually takes place. Another principal QE degradation mechanism, oxidation by residual gases, has recently been used to study the evolution of a photocathode's surface and its impact on photoemission in a controlled way. Significant progress has been made in understanding the chemical reconstruction of the cesiated GaAs surface upon exposure to molecular oxygen [46–48], but only recently has a kinetic model [49] based on experimental data [48] explained nonexponential QE degradation dependencies by taking into account an intermediate, physisorbed, state of the oxidizing gas molecules. We consider this an important refinement, because neglecting this state leads to inaccurate estimates of the surface reaction rates. More importantly, the kinetic model defines a universal QE degradation metric as a set of three reactions rates (physisorption, desorption, irreversible oxidation) [49], instead of widespread but ambiguous lifetime expressed by pressure over a time integral in Langmuir units.

A limitation of the kinetic model is that only abrupt changes in the electron affinity are assumed to drive a surface site from a photoemissive to a nonphotoemissive state. This can be remedied, but the adoption of a composite reaction-rate lifetime metric will ultimately depend upon its practical utility in the field. Future models of QE degradation will need to incorporate the net result of reversible and irreversible surface chemical reactions, each with its own rate (activation energy) [49] and effect on electron affinity [50]. Since the known processes responsible for QE degradation are limited to a few monolayer depths, optical and bulk electronic properties of a photocathode are not affected. Therefore, the link between the future QE degradation models and other photocathode metrics resides in considering the time evolution of a microscale spatially modulated $E_a + E_g$. It is worth noting that oxidizing a cathode usually increases the electron affinity only after a certain submonolayer threshold. For coverages below the threshold, an activation, or enhancement of longer wavelength response due to lowering of the electron affinity, is observed [51], but these effects will likely manifest differently (if at all) in the nanostructured cathodes advocated below. Hence, careful consideration is required to predict, for example, transverse emittance changes during oxidation of a photocathode illuminated by a laser with a wavelength close to photoemission threshold. Experimental validation of future comprehensive QE degradation models should be based on precise continuous monitoring of the full spectral response evolution (as well as background gas composition using a residual gas spectrometer tool) during the photocathode degradation

process, correlated with surface-state diagnostics [47], and beam-emittance measurements.

A. Impact of photocathode performance on XFELs

Numerous studies, mostly based on the Ming-Xie gain-length parameterization method [52], show how reductions in emittance improve both peak output power and photon energy of various self-amplified stimulated emission (SASE) XFEL designs [53]. The goal for a SASE XFEL design is to achieve high electron-beam energy γ with high peak current I_{peak} while maintaining low emittance $\varepsilon_{n,\text{rms}}$, and small energy spread σ_δ so that x-ray output power $P(z)$, at x-ray radiation wavelength λ_{fel} , grows exponentially with undulator distance z until saturation is reached either at saturation length L_{sat} or the end of the undulator (L_u) [54]. The relations governing XFEL performance are as follows:

$$P(z) = P_0 \exp(z/L_g)|_{z < \min(L_u, L_{\text{sat}})}, \quad (1)$$

$$L_g \approx \frac{\lambda_u}{4\pi\sqrt{3}\rho}, \quad (2)$$

$$\varepsilon_{n,\text{rms}} < \gamma \frac{\lambda_{\text{fel}}}{4\pi}, \quad (3)$$

$$\sigma_\delta = \frac{\sigma_\eta}{E_b} < \rho \approx \frac{1}{4} \left(\frac{I_{\text{peak}} \lambda_u^2}{2\pi^2 I_A \beta \varepsilon_{n,\text{rms}} \gamma} K^2 \right)^{1/3}, \quad (4)$$

where K is the undulator field strength, ρ is the FEL parameter, L_g is the FEL gain length, and $I_A = 17.5$ kA is the Alfvén current.

A case study (based on the Ming-Xie formula) is presented here for parameters in Table II equivalent to those of LCLS-II/HXR [54]. Figure 3 shows that a reduction in normalized emittance enables higher x-ray output per pulse and significantly higher photon energy for a constant electron-beam energy $E_b = 15$ GeV and fixed undulator length $L_u = 140$ m. This example illustrates why emittance reduction is usually a high priority: it provides strong

TABLE II. LCLS-II/HXR case study parameters.

Parameter	Definition	Value
E_b	Beam energy	15 GeV
σ_η	Energy spread	1.5 MeV
L_u	Undulator length	140 m
λ_u	Undulator period	26 mm
I_{peak}	Peak current	3.5 kA
β	Mean beta	30 m
Q_b	Bunch charge	100 pC

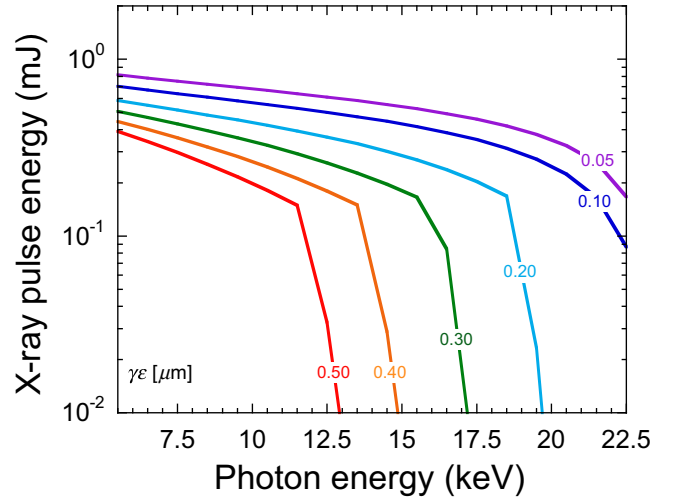


FIG. 3. Illustrating the important role of emittance in XFEL performance: x-ray pulse energy (mJ) vs output photon energy (keV), using the analysis of Ref. [52] and machine parameters of LCLS-II/HXR [54] shown in Table II. A reduction in normalized emittance is seen to increase peak photon energy.

leverage for achieving better SASE XFEL performance [55]. Additionally, lasing becomes increasingly sensitive to emittance growth at higher x-ray photon energies, as shown in Fig. 4. Historically, emittance in the accelerator was dominated not by the cathode thermal emittance but by the beam dynamics in the photoinjector [56]. Emittance

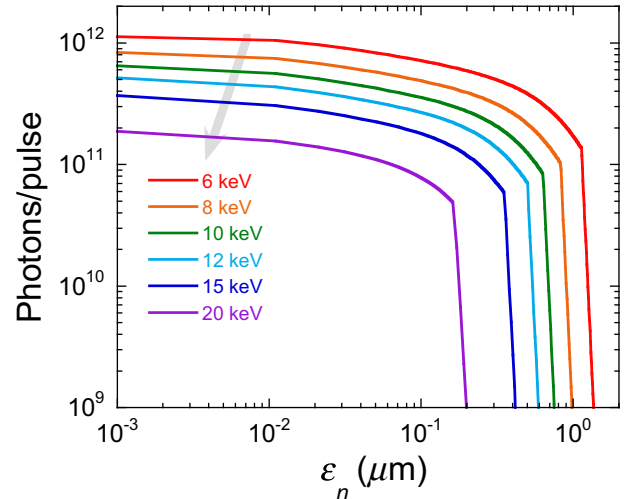


FIG. 4. X-ray output (photon per pulse) as a function of normalized emittance for the various photon energies indicated (for bunch charge $Q_b = 100$ pC and a fixed electron-beam energy of 15 GeV). This illustrates why submicron emittance is typically required for lasing near approximately 22 keV and that the sensitivity to emittance increases at higher photon energy. The direction of the gray arrow indicates increasing photon energy (keV).

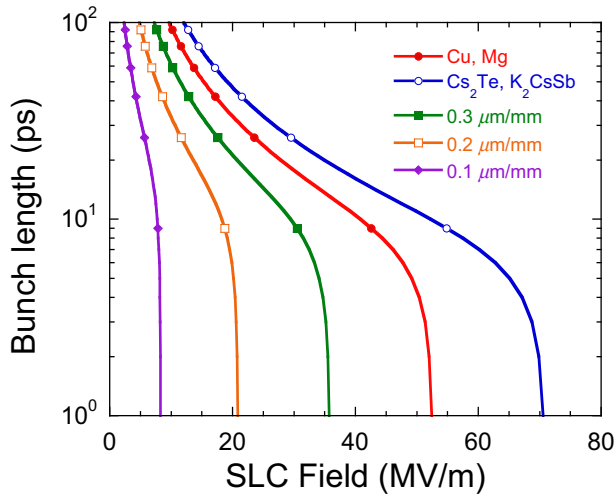


FIG. 5. Curves of constant thermal emittance at the cathode relating emitted bunch length with space-charge-limit field E_{SCL} (defined as the minimum field strength required to extract the entire bunch), showing that emittance plays a role in photoinjector beam dynamics that affect SASE XFEL machine architecture: for a given bunch charge $Q_b = 100$ pC, reduced thermal emittance allows for shorter bunch lengths, which, in turn, improves machine performance by relaxing bunch compression requirements.

reduction at the cathode was, therefore, not a high priority since such efforts would be inevitably negated.

Modern photoinjector designs, however, have evolved to the point where the intrinsic emittance (that is, the contribution to the emittance due to the cathode, elsewhere termed thermal emittance as an equivalent designation [6]) limits both existing and future XFEL designs and upgrades [39]. The impact of suppressed cathode thermal emittance on future machine upgrades, can be illustrated as in Figs. 5 and 6. Figure 5 shows the photoinjector tradeoff between cathode response time (electron bunch length) and field gradient: for a given field at the cathode, suppressed thermal emittance allows for shorter bunch lengths [57]. Shorter bunch length out of the photoinjector is beneficial in terms of machine cost and complexity because it reduces downstream bunch compression ratios. Figure 6 shows that for a desired x-ray performance target (approximately 22 keV in the LCLS-II/HXR example), emittance reduction allows lasing at a lower electron-beam energy despite increased relative energy spread. Since lower electron-beam energy equates to significant savings in both cost and footprint of a large-scale user facility, the high priority and focus on emittance suppression is justified. Furthermore, in terms of existing facility upgrades, cathodes are generally much easier to improve and upgrade than other critical components such as linacs, undulators, or periodic focusing magnets, etc. Cathode optimization, therefore, is increasingly viewed as a straightforward and cost-effective

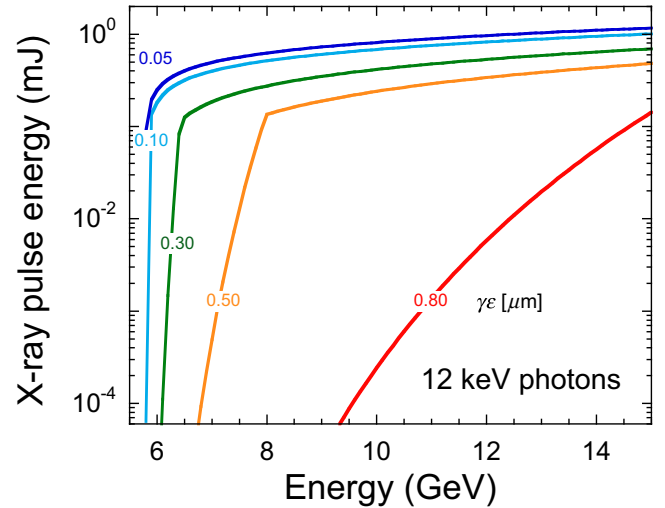


FIG. 6. X-ray pulse energy (mJ) at 12 keV as a function of electron-beam energy for several values of normalized emittance, demonstrating that lasing at this performance target can be achieved at lower electron-beam energy if emittance is suppressed.

upgrade path for existing facilities while also enabling greater trade space for future XFEL designs.

B. Model of QE and emittance

Quantum efficiency and emittance $\varepsilon_{n,\text{rms}}$ have received significant attention in efforts to develop predictive models. The phenomenological three-step model of Spicer [36,37,58] has not only proven useful in predicting QE, but also in evaluating emittance [10,59], a feature common to the similar moments-based models [17,23] applied to metal photoemitters. The underlying physics for metal photocathodes was shown by Dowell and Schmerge [10] to enable expressing QE as a function of emittance $\varepsilon_{n,\text{rms}}$, leading to the Dowell-Schmerge relation

$$\text{QE} \propto \varepsilon_{n,\text{rms}}^4 \quad (5)$$

that holds reasonably well for photon energies $\hbar\omega$ near the Schottky-reduced work function $\phi = \Phi - \sqrt{4QF}$. It demonstrates that improvements in QE and reductions in emittance are oppositional: both increase with photon energy [10,35]. Moreover, QE generally increases as response time increases [12,25,26,38,60,61], so for conventional bulk metal photocathodes, laser wavelength and pulse duration are the only adjustable parameters available.

Treating semiconductors requires additional physics (e.g., band bending, barrier shape, and effective-mass variation), and has not yet resulted in a relation with the aesthetic simplicity of Eq. (5). Nevertheless, a reconsideration of QE using the moments model makes probable a similar linkage between QE and $\varepsilon_{n,\text{rms}}$. Semiconductors such as Cs_3Sb and K_2CsSb can be treated by the

moments model if modified by physics related to effective mass, band-gap modifications, band bending, and a more complex tunneling barrier [62]. Reflectivity $R(\omega)$ and laser-penetration depth $\delta(\omega)$ are evaluated using variants of a Lorentz-Drude model, and the relaxation time $\tau(E)$ governing the mean free path $l(E)$ of photoexcited electrons accounts for e - e and e -ph scattering contributions. QE is then a ratio of currents and of the form

$$\text{QE} = \{1 - R(\omega)\} \frac{M_1(k_x)}{2M_1(k)|_{D=1, f_\lambda=1}}, \quad (6)$$

where $k_x = k \cos \theta$, $D(E)$ is the transmission probability for emission, f_λ governs the loss of electrons due to scattering in the fatal approximation, and

$$M_n(k_x) \equiv \frac{2}{(2\pi)^3} \int k_x^n f(\vec{k}) d\vec{k}. \quad (7)$$

Other factors account for the occupation of the initial and final scattering states.

Semiconductor QE differs from metals. For metals, the initial and final occupation factors are (as temperature $T \rightarrow 0$)

$$f_{FD}(E)[1 - f_{FD}(E + \hbar\omega)] \rightarrow \Theta(\mu - E)\Theta(E - \mu + \hbar\omega), \quad (8)$$

where E is the electron energy, f_{FD} is the Fermi-Dirac distribution, and $\Theta(x)$ is the Heaviside step function. Additionally, the transmission probability is a step function, or $D(E) = \Theta(E - \mu - \phi)$, where μ is the Fermi energy and $\phi = \Phi - \sqrt{4QF}$ is the Schottky-reduced work function in response to field $F = q\mathcal{E}$, and $Q = 0.36$ eV nm. Accounting for absorption, transport and emission for metals, therefore, gives rise to (compare Ref. [10])

$$\text{QE} \approx (1 - R) \frac{\int_{k_m}^{k_F} k^2 dk \int_0^{x_m} (\hbar k x / m) f_\lambda(x, p) dx}{2 \int_{\sqrt{k_F^2 - k_\omega^2}}^{k_F} k^2 dk \int_0^1 (\hbar k / m) dx}, \quad (9)$$

where $x = \cos \theta$, $x_m = \cos \theta_m$, $\hbar^2 k_F^2 / 2m = \mu$, $\hbar^2 k_m^2 / 2m = \mu - \hbar\omega$, and $\hbar^2 k_\omega^2 / 2m = \hbar\omega$. The integrand vanishes for $x = x_m$. Also, $f_\lambda(\cos \theta, p) = \cos \theta / (\cos \theta + p)$, where θ is the angle with respect to normal to the surface, and $p = \delta(\omega) / l(E)$, where $l(E) = \hbar k(E) \tau(E) / m$ is the mean free path and $E = \hbar^2 k^2 / 2m$. The evaluation of Eq. (9) can be shown to be proportional to $(\hbar\omega - \phi)^2$ to leading order.

How semiconductors differ is as follows. First, the photoexcited electron must have an energy above the band gap E_g . Second, assuming the barrier at the surface has an increased triangular shape as per Spicer, the Schottky barrier (image charge) transmission probability $D(E)$ is the triangular $D_\Delta(E)$ treated by Fowler and Nordheim [63] (but see Ref. [64]). Lastly, a magic window exists for

semiconductors, where scattering effects are not fatal as for metals. For semiconductors then,

$$\text{QE} = (1 - R) \frac{\int_{E_a}^{\hbar\omega - E_g} E dE \int_{x_m}^1 x dx D_\Delta[Ex^2] f_\lambda(x, p)}{2 \int_0^{\hbar\omega - E_g} E dE \int_0^1 dx}, \quad (10)$$

where $x_m = \sqrt{E_a/E}$ with E the energy of the photoexcited electron. The transmission probability for an electron with normal energy E_z for a triangular barrier is [24,65]

$$D_\Delta(E') \approx \frac{4[E'(E' - E_a)]^{1/2}}{(E'^{1/2} + (E' - E_a)^{1/2})^2}, \quad (11)$$

where $E' = E \cos^2 \theta$. Approximating the angular integration by the trapezoidal approximation,

$$\int_{x_m}^1 x D(Ex^2) \frac{x}{x+p} dx \approx \frac{\sqrt{E} - \sqrt{E_a}}{2(1+p)\sqrt{E}} D(E), \quad (12)$$

where $p = \delta(\omega) / l(E_a)$ as the lower bound, leading to

$$\text{QE} \approx C(1 - \eta)(1 - \sqrt{\eta})D(E_m), \quad (13)$$

where $\eta = E_a/E_m$. Note that $C \propto (1 - R)/(1 + p)$ and includes other factors that affect QE [e.g., a scale factor to account for the underestimation of QE by using Eq. (12)]. In terms of the dimensionless $s^2 = (\hbar\omega - E_g - E_a)/E_a$ then QE is

$$\text{QE} \approx \frac{2Cs^5}{(1 + s^2)(1 + \sqrt{1 + s^2})(s + \sqrt{1 + s^2})}. \quad (14)$$

Contrast Eq. (14) with the parametric form of Spicer [58] that is equivalent to

$$\text{QE}_{\text{Spicer}} = \frac{(\hbar\omega - E_g - E_a)^{3/2} G_o}{(\hbar\omega - E_g - E_a)^{3/2} + \gamma} \equiv \frac{s^3 G'_o}{s^3 + \gamma'}, \quad (15)$$

where G_o is a constant. Such a parameterization gives different values of $(G_o, \gamma, E_g + E_a)$ for different measurements, e.g., (0.186, 0.699, 2.04) for Spicer [58] and (0.397, 1.70, 1.88) for Taft and Philipp [66], as per Ref. [24]. By comparison, Eq. (14) performs well in the intermediate energy regime where s is of order unity, but asymptotically has an s^5 dependence as $s \rightarrow 0$ and an s^1 dependence for $s \gg 1$. Equation (14) is superior for modeling the quantum efficiency of Cs_3Sb for data taken by Spicer [58] as well as Taft and Philipp [66], as shown in Fig. 7: differences are accounted for by p , for which the smaller C associated with Spicer implies a larger p and, therefore, a smaller mean free path. Consequently, whereas $\text{QE} \propto (\hbar\omega - \phi)^2$ for metals, for semiconductors, the power p differs from 2. Accounting for a scattered electron contribution will also affect the overall scale, but

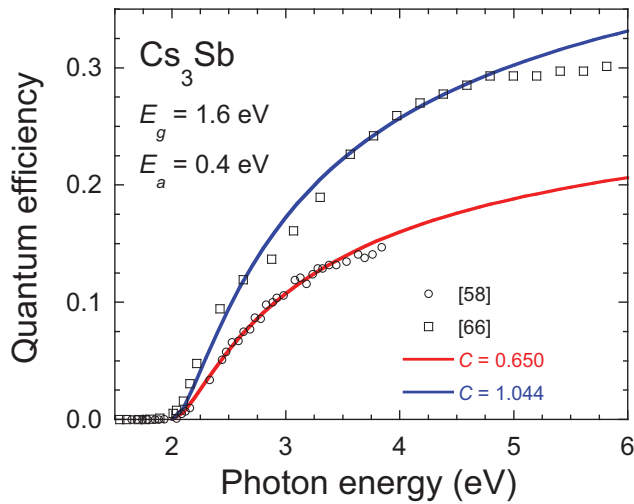


FIG. 7. Comparison of the data of Spicer [58] and Taft and Philipp [66] for cesium antimonide (Cs_3Sb) (symbols) compared to Eq. (14) with $C = (1 - R)/(1 + p)$.

can be accounted for by amending QE with a wavelength-dependent coefficient [35]. Thus, the relationship between QE and $\varepsilon_{n,\text{rms}}$ for semiconductors will likely show a power-law relation as in Eq. (5) but with a different power. Stating that QE and $\varepsilon_{n,\text{rms}}$ are coupled for bulk materials in general is therefore warranted.

Numerical QE calculations are vetted against data in the literature, as shown in Fig. 8. Although Eq. (14) presumes a constant value of C [it should vary because $R(\omega)$, $\delta(\omega)$, and $l(\hbar\omega - E_g - E_a)$ vary], the correspondence is good. Compared to more recent data for K_2CsSb , albeit with the presence of N graphene layers [71], with $N = 5$ and 8, is shown in Fig. 9. Adding a graphene layer may modify the transmission probability [72] and will be treated separately [64], although note that for photon energies in excess of twice the band gap, the magic window [38] of semiconductors is surmounted and electron-electron collisions begin to shorten the mean free path $l(E)$.

Note that C contains numerous internal factors, specifically the reflectivity and the ratio of the laser-penetration depth $\delta(\omega)$ to the mean free path $l(E)$, and implicitly includes the fraction of the illuminated surface that is emitting. In Eq. (14), these factors cannot be separated, but a proper numerical evaluation of Eq. (10) using actual optical data, or even a Lorentz-Drude model, will begin showing the impact of graphene layers on the electron emission, and such a study is in progress. Interestingly, although the theory line of Fig. 9 closely matches the 8L and 5L data lines up to $\hbar\omega \approx 3$ eV, a departure between theory and data occurs, with the theory increasing as the data decreases until by $\hbar\omega \approx 4.6$ eV there is a factor of $2.5\times$ difference between them. The nature of a graphene layer on a copper surface was therefore examined theoretically, and the analysis is separate [64].

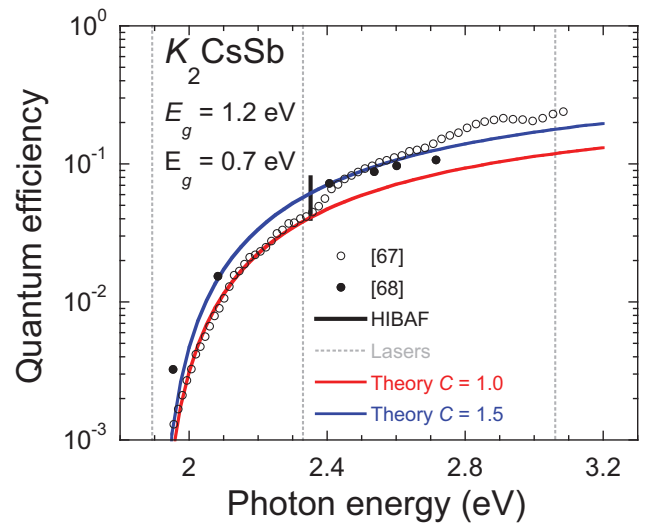


FIG. 8. Comparison of the data of Bazarov *et al.* [67], Michelato *et al.* [68] (represented after Ref. [69]), and the HIBAF experiment [70] compared to Eq. (14) with $C = (1 - R)/(1 + p)$. The vertical dashed lines correspond to common laser wavelengths and are (from left to right) for $\lambda = 655, 532,$ and 405 nm.

III. MATERIAL DESIGN APPROACH

The linked metrics of conventional photocathodes described above are a consequence of transport through an unstructured bulk and a surface that, when it impedes emission of thermalized carriers, acts only to provide an obstacle over which electrons must pass. Several of the most significant developments in semiconductor nanofabrication and heterostructure, nanocrystalline, and

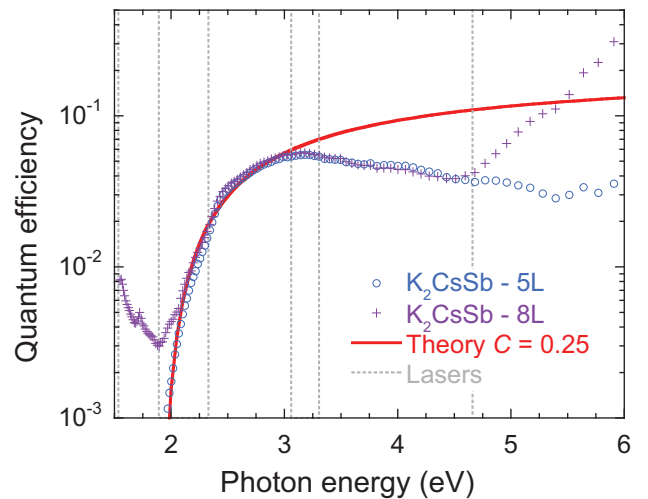


FIG. 9. Comparison of Eq. (14) with $C = (1 - R)/(1 + p)$ to recent measurements of K_2CsSb with N graphene layers, with $N = 5$ or 8. Vertical dashed lines correspond to common laser wavelengths and are (from left to right) for $\lambda = 655, 532, 405, 375,$ and 266 nm.

superlattice fabrication capabilities go well beyond this and remain underutilized [73–77]. These include utilizing: compositionally graded semiconductor materials with widely tunable band gaps; heterostructure architectures, quantum wells, quantum tunneling, enhanced carrier transport using internal electric fields and superlattices consisting of nanoscale structures (e.g., quantum dots where quantum confinement restricts emission from discrete energy levels). These emerging capabilities allow, to varying degrees outlined below, tailoring of composition and electronic structure to influence the fundamental mechanisms of photoemission: absorption, transport, and emission. Importantly, the requisite material synthesis capabilities have recently matured over roughly the same timescale as theoretical techniques have emerged allowing for computational studies of photoemission physics from these new material systems. A comprehensive material-centric approach to cathode design suggests, at minimum, the close integration of four key elements: (i) computation materials physics models; (ii) nanoscale material synthesis techniques; (iii) *in situ* surface-science characterization; and (iv) correlation of specific material properties (such as electronic structure) with electron-beam-emission characteristics (such as thermal emittance). Each area is discussed below by examining recent results that may benefit cathode design.

A. Computational materials physics and modeling tools

A prerequisite for exploiting design opportunities offered by band structure engineering (BSE) of quantum wells, dots, nanocrystals, graphene layers, heterostructures, and graded composition heterostructures, is the coupling of computational physics models to experimental investigations and evolving applications. For example, QE alone is no longer the primary metric, but is one of a number of metrics, such as QE plus low thermal emittance plus long cathode lifetime and short response time [12,54,78]. The modeling framework being pursued herein conjoins computational materials physics frameworks such as density-functional theory (DFT), tight binding methods, and electronic structure calculations [79], with field and photoemission theories (e.g., moments-based emission and transport models coupled with quantum-mechanical transfer matrix methods [35,72,80]). Predicting photocathode performance for graded compositions with heterostructures or quantum features has necessitated the creation of new theoretical models encompassing both computational materials physics and emission and transport, broadly characterized by (i) quantum effects such as resonant tunneling, photoexcitation from discrete energy levels, and quantum-mechanical emission models from discrete energy levels; (ii) optical and material effects that govern the nature and location of absorption and excitation,

as well as band bending and surface barrier properties; (iii) heterostructure effects that govern normal energy transport, but also impact surface ruggedness, influence emission barrier properties and emission time; and (iv) and doping profiles and their effect on internal electric fields.

The DFT, tight binding, and electronic structure models provide theoretical replacements to historically absent, ad hoc, and empirical relations for material and optical parameters in the moments-based (distribution) approach to modeling photocathodes. They provide the band edge relations needed by transfer matrix approaches for the evaluation of resonant and quantum effects in heterostructures as shown in Fig. 10. They also assist in developing models of quantum wells and dots and the laser-excitation interactions needed by the more phenomenological theoretical models under development.

Computational materials physics methods include various approaches that can be used to find the effect of material properties, heterostructure constructions, and applied fields on the emission properties of engineered confined-electron structures (including quantum wells and dots). Each method operates in a spatial regime that has applicability to heterostructures for treating potential variation at interfaces at an atomic level up to modeling current flow, carrier transport, and mesoscale features. Density-functional theory is perhaps the best known method, but other computational approaches include DFT-Hartree-Fock (for heterostructure and nanoscale features), molecular dynamics (for atomic scale simulations), dissipative particle dynamics and lattice Boltzmann or cellular automata methods (for mesoscale simulations), continuum mechanics and fluid dynamics, and simulations based on macroscopic transport equations (for finite differences and finite elements). A collection of interesting discussions concerning materials simulation at different spatial scales and their coupling using computational methods are given in Ref. [81]. These suggest the following priorities:

(a) *Near-term*: Incorporation of computational materials physics methods to treat band-gap tailoring, doping, effective-mass variation, optical parameters controlling laser-penetration depth and reflectivity, field penetration, and material parameters in beam optics codes

(b) *Long-term*: Modeling of band bending and band-gap variation by graded stoichiometric variation and doping to tailor photoabsorption characteristics; heterostructures, doping, intrinsic electric fields, and quantum-confinement models and their impact on electron emission behavior as related to QE, emittance, and pulse-shaping requirements

B. Nanomaterial synthesis and fabrication

Engineered stoichiometry and/or quantum confinement by using quantum well heterostructures or a lattice

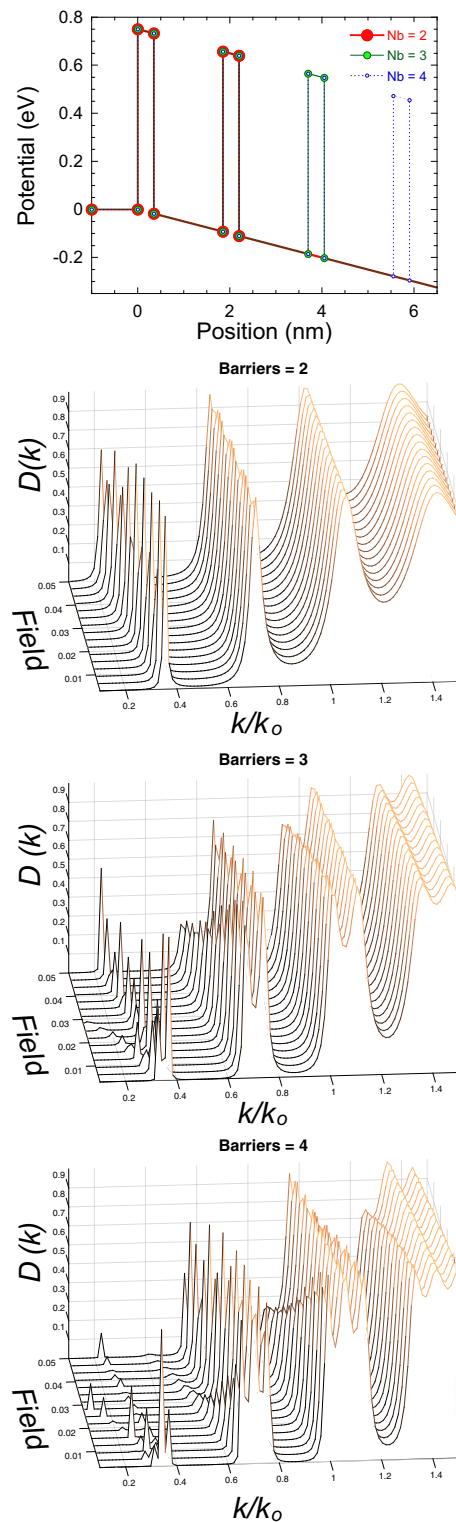


FIG. 10. Effects of heterostructure barriers on filtering and transmission probability. (Top to bottom) Potential as a function of position for two to four barriers of height $V_b = 0.75$ eV, barrier width of 0.35 nm, and well width of 1.5 nm. Transmission probability $D(k)$ as a function of momentum k with $\hbar^2 k_o^2 / 2m = V_b$ and field in [eV/nm] for two, three, and four barriers in a waterfall format (each line represents a different field).

of quantum dots, introduces absorption, transport, and emission processes that can potentially decouple otherwise competing metrics by discretely controlling the excitation and emission energy levels, tailoring the band gap, varying the internal electric fields, adjusting the effective-mass variation, and specifying the dielectric and optical properties. Among the many challenges in incorporating nanostructure in photocathode design is understanding how the available features influence parameters governing photoemission (such as reflectance, laser absorption, laser-penetration depth, electric-field penetration, and band bending), such that new properties and processes emerge that enhance photoemission (e.g., fast and direct photoexcitation near the surface from confined energy levels in quantum wells or dots).

1. Quantum confinement in cathode materials

Classes of reduced dimensionality and corresponding (idealized) electronic energy levels are shown schematically in Fig. 11 spanning from bulk (3D) materials to quantum wells (2D) to quantum wires (1D) to quantum dots (0D). Quantum dots (QDs) are single semiconductor nanocrystals on the order of 2–20 nm in size, as depicted in Fig. 12, that exhibit a number of properties highly relevant to photocathodes, such as discrete electronic states [83,84], relaxation of carrier momentum constraints [85], and precise tuning of electronic structure and carrier behaviors [86]. These emergent properties are a direct consequence of quantum confinement and QD synthesis techniques have now matured such that experimental photoemission studies can begin in earnest [87]. Interestingly, the applications which first motivated QD development (wavelength tunable phosphors) required suppression of photoionization, whereas photoemission requires the exact opposite: photoionization is a necessary step in electron emission. The small volume defined by the dot produces a natural

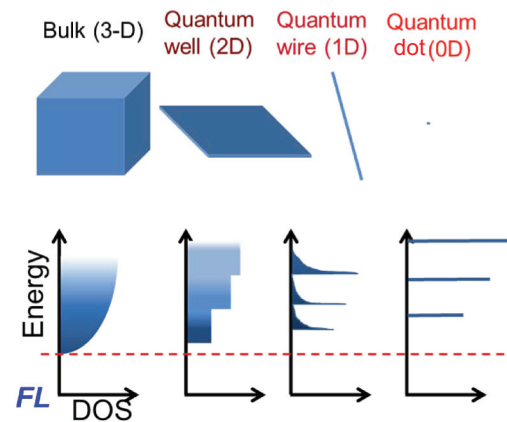


FIG. 11. Relation of dimensionality to energy level discreteness, from bulk 3D to quantum dots.

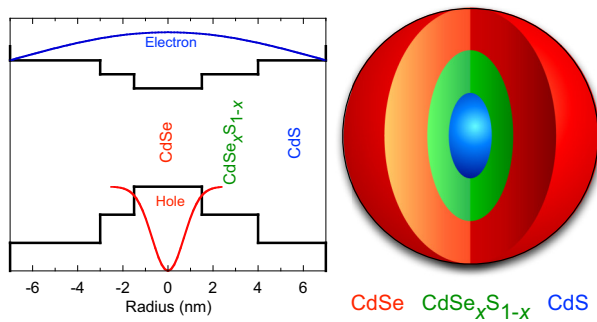


FIG. 12. Energy band diagram of a quantum dot and the electron and hole wave functions (*left*), based on Ref. [82] and the depiction of a sophisticated QD heterostructure (*right*).

tendency toward photoionization, which can be exploited (rather than suppressed) to favor photoemission.

The tuning and optimization of these material systems, examples of which are indicated in Figs. 12 and 13, occur by manipulating size, geometry, and composition of the constituent nanocrystals. Strictly controlled synthesis allows assembly into 3D superlattices [73,76] from individual QD components, which can exhibit energy spread on the order of kT as measured via single QD photoluminescence [88,89]. Because these properties can be highly controlled during synthesis (and validated via characterization) their tunability allows an engineering approach to designer photocathode materials. While QDs share similarities to bulk conventional semiconductor cathodes, carefully prepared and treated nanocrystals are also not as chemically reactive, which further motivates their investigation for electron-beam generation, where low doses of residual gases in the vacuum environment can often corrupt cathode films [14,90].

Until recently, QDs were not practical for photocathode applications due to the lack of methods for preparing

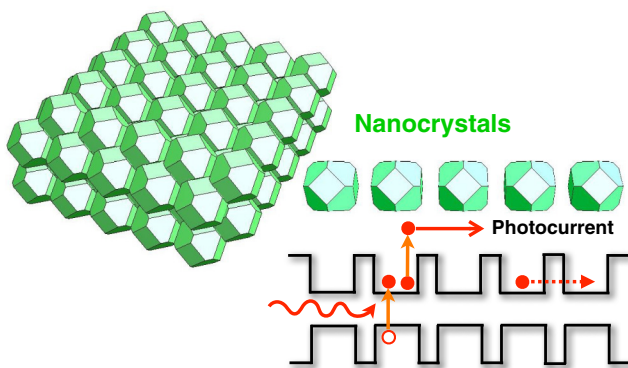


FIG. 13. 3D lattice schematic showing potential energy for electrons and holes in a periodic array undergoing photoexcitation, resonant tunneling (dashed arrow) and photoexcited transport (solid arrow), based on Ref. [74].

highly conductive QD films that can accommodate charge injection, although measuring ionization potential and effective work function of nanocrystals has emerged as a powerful technique for the investigations of nanocrystalline films [91,92]. Largely driven by the needs of QD-based photovoltaic and light-emitting technologies, conductive films can now be achieved by ligand exchange to small molecules [93,94] or by infilling of the inter-QD space by metal oxides via atomic layer deposition (ALD) [95,96]. These sophisticated methods to control QD surfaces and interfaces, including film conduction, have resulted in the emergence of practical QD-based technologies such as full-color displays [97], high-performance solar cells [98,99], light-emitting diodes [82,100,101], and photon detectors [102,103]. The optimization of electronic excitation and transport in each of these demonstrated applications suggests they could be applied to photocathodes.

Examination of multilayer QD films as photocathodes has already begun and has shown a promising response in a low-gradient DC electron gun configuration [87]. Photoemission from PbSe, CdSe, CdSe/CdS has been studied as a function of the excitation photon energy, intensity, and pulse duration. The dominant mechanism in the multiphoton excitation regime was shown to involve short-lived hot electrons, as determined from carrier lifetime studies carried out by varying excitation pulse width. For short-pulse emission, QDs have the potential to become charged if a means for replenishing the electrons is not provided. Thus, electrically conductive films must be prepared by spin-coat methods [104–106], using a layer-by-layer approach with treatments to remove the original surface ligands to enhance charge mobility.

Photocurrents as high as 1 nA are achieved using 800-nm excitation (100-mW excitation power), whereas higher-energy photons can produce up to 2 to 10 nA of current at 10 to 50 mW. The experimental trends are highly reproducible, as shown in Fig. 14, particularly for 400- and 266-nm excitation where nearly all photons are absorbed by the PbSe film. By energy conservation, a single photon (energy of 4.66 eV or less) cannot directly induce photoemission from PbSe: consequently, two to four photons must be involved per electron, depending on excitation wavelength. Reproducibility and appreciable photocurrent (3 to 5 \times higher QE than atomically clean copper) were obtained at all wavelengths, including 800 nm. A potential advantage of using QDs for cathode applications is the wide variety of material compositions available, including multicomponent heterostructures, whose electronic structure can be tailored to match design-specific needs [86]. Thermal emittance measurements of these films are planned [78] with the goal of correlating this metric with QD shape and composition.

To illustrate some possibilities, a film of CdSe/CdS core/shell heterostructure QDs is fabricated (using the

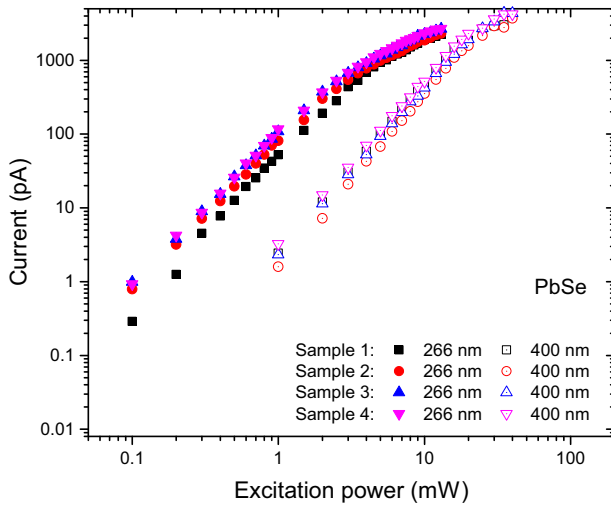


FIG. 14. Electron-beam emission from QD films [87]: good reproducibility of photoemission data across multiple samples of PbSe at both 400- and 266-nm excitation.

synthesis procedures outlined in Ref. [87]) to compare performance with single-component CdSe QDs. QD-size-dependent photoelectron spectroscopy shows [107] that photoelectron yield *increases for smaller QDs*, explained as a consequence of the electron wavefunction extending outside of the QDs. Note that for QDs, electron transport following excitation is very different from conventional cathode materials because the wave function is already near the vacuum surface barrier. The CdSe/CdS heterostructures exhibit so-called quasi-type-II band alignment that promotes the spatial separation of electrons from holes via reduced wavefunction overlap [82]. Because of reduced electron-hole Coulomb interaction, removing electrons from these core/shell structures into the vacuum should be more efficient than in the case of core-only CdSe QDs, and this is indeed observed experimentally.

For this core/shell composition and size (3.8-nm core radius, band gap of 1.86 eV), the top of the valence band is 6.69 eV below the vacuum level. Therefore, two 4.66-eV photons are required for the generation of each photoelectron and this is apparent when plotting emission as shown in Fig. 15. The maximum photocurrent is enhanced more than threefold to 6.9 nA with the heterostructuring technique compared to core-only CdSe QDs at very modest laser powers of 7.7–7.9 mW, showing the feasibility of optimizing cathode performance. All QD samples examined in this study exhibited quantum efficiencies exceeding that of atomically clean copper. Although this is several orders of magnitude lower than the efficiency of the best performing bulk semiconductor thin-film cathodes, such as Cs₃Sb [24] and K₂CsSb [108,109] or NEA GaAs [110], these are only preliminary studies with limited optimization. Importantly, these films were briefly handled in air while loading into a load-lock chamber, a procedure

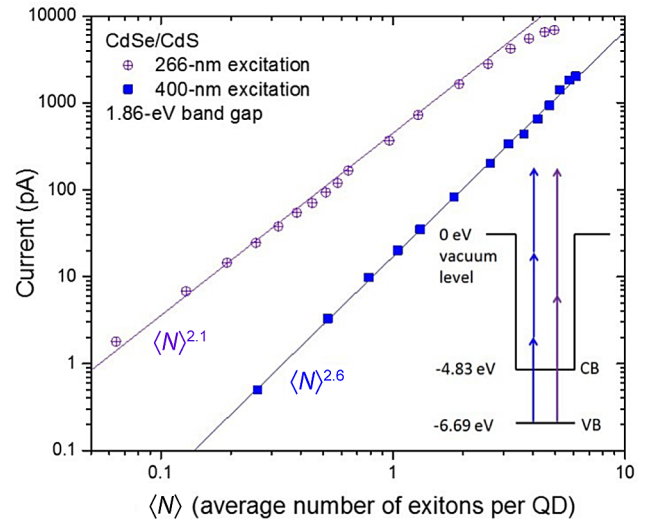


FIG. 15. Photocurrent vs average number of excitons per QD $\langle N \rangle$. The photocurrent scales approximately as the second and third power of $\langle N \rangle$ for 266- and 400-nm excitations, respectively, consistent with the energy band diagram shown in the inset.

that would not be tolerated by bulk semiconductor cathodes, whose efficiencies degrade dramatically even under $< 1 \times 10^{-10}$ Torr vacuum conditions [14,110]. Indeed, the QD films showed no deterioration in performance after several weeks in 2×10^{-8} Torr vacuum. Storage in air for two months resulted in only a 55% drop in the maximum photocurrent value when excited at the same power with 266-nm photons, comparable to copper in air [111].

2. Heterostructures in cathode materials

Heterostructure and superlattice layers introduce discrete energy levels and quantum effects (e.g., resonant tunneling) as suggested by multibarrier structures in Fig. 10, evaluated using an Airy transfer matrix approach [65], where the addition of more barriers suppresses transmission between resonant peaks, and puts greater structure on the peaks themselves: such a structure would be smoothed by the rounding of physical barriers as evaluated using, e.g., density-functional methods. Additionally, a wide band-gap material used as a protective cap atop a chemically sensitive surface may, if the bands are aligned correctly, have little impact on the QE. Fabrication capabilities include the design of pristine, ordered layers such as graphene (e.g., Fig. 16) or other 2D films at the surface, which in addition to modifying transport at the surface can also impact surface sensitivity to contamination and degradation [112].

The first examples of successful integration of pristine few-layer graphene coatings with photoemission cathodes has occurred [114] in the form of atomically clean bulk copper (Gr-Cu) applied to graphene photocathodes [113] and the growth of high QE K₂CsSb on suspended

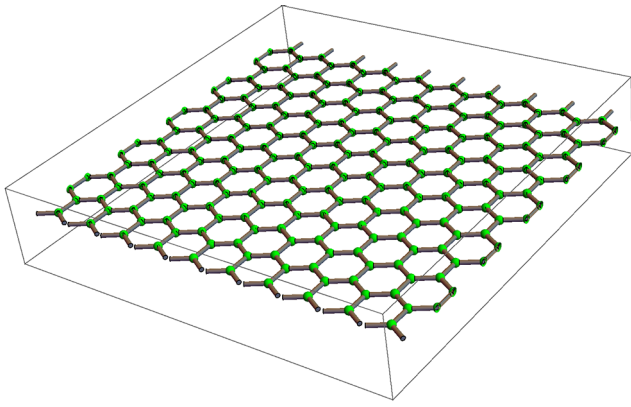


FIG. 16. Graphene consists of a single layer of carbon atoms in a close-packed 2D honeycomb lattice (boron nitride, discussed elsewhere, shares a similar lattice). Graphene and other 2D layers exhibit many unique properties and the tunneling characteristics are a result of charge density, as recently studied in conjunction with its performance as a protective gas barrier layer [112,113].

transparent graphene substrates [71,115]. In the copper study, the spectral response of the Gr-Cu system was measured as a function of the copper crystal face and thickness of graphene. For monolayer graphene coatings, a reduction in work function Φ and an increase in QE is observed for all faces with the greatest effect occurring for the $\langle 110 \rangle$ case.

In stark contrast to usual over-the-barrier emission processes (which govern most photocathodes as well as all thermionic cathodes), resonant tunneling and reflectionless processes can substantially increase transport through barriers and over heterostructure barriers and wells [65].

The distribution of electrons that would be filtered through the heterostructures at the surface, or serve as the energy levels in quantum dots that are directly photoexcited, can be modified or controlled by band-gap engineering using ALD, pulsed laser deposition (PLD), or MBE. These methods can provide control over the stoichiometry of the bulk material where photoexcitation and transport to the surface occurs or the engineering of discrete energy levels governing emission from quantum wells and dots. Such control is similar to, but beyond, simple band bending as a result of bulk doping. An engineered stoichiometry or a purposely created quantum-confined structure, such as a quantum well or a lattice of quantum dots, creates transport and emission processes that can potentially decouple otherwise competing metrics by controlling the discrete energy levels, tailoring the band gap, adjusting the effective-mass variation, doping, and specifying the dielectric and optical properties. Thus, it is possible to control many of the features upon which photoyield traditionally depends (such as reflectance, laser absorption and penetration depth, and field penetration and band bending) while enabling new processes (fast and direct photoexcitation near the surface from confined energy levels in quantum wells and dots).

Quantum confinement in 1D and 2D governs the unique behavior of resonant tunneling diodes [116] and LEDs and provides a practical model for employing similar resonant behavior in nanoengineered photocathodes. Engineered barrier structures can introduce resonances or quantum wells imposing nontrivial structure on the transmission probability $D(E_k)$ that filters electron emission past the surface barriers. The theoretical analysis of such effects are reliant on representations of the wave function that span the entire potential region and require numerical approaches for analysis [117,118]. Examples are shown in Fig. 10 for representative potentials involving resonant transmission where band bending at the surface caused by field penetration introduces energy levels of a separate character but with analogous effects and which are time dependent in conjunction with the rf fields under which photocathodes would operate. The related transmission probabilities show resonances and structure very different from the step-function transmission probability generally used in three-step [10,38] or moments-based models [15,24] of photoemission by allowing significant transmission in narrow bands below the barriers, and reduced transmission in bands above the barriers themselves (k/k_0 in Fig. 10 marks the transition from below to above barrier transport). Different behavior than that assumed in QE models such as the three-step or moments model is evident. The restrictions or modifications imposed on transmitted electrons provides an opportunity for energy selection that may be attractive even though such a structure may degrade QE. The impact on either emittance or response time may have the potential to be more advantageous in some circumstances.

3. Advanced thin-film semiconductors and band-gap engineering of photocathode materials

In the context of thin-film photocathode materials, there are methods for utilizing nanoscale engineering to modify material properties that could favorably impact overall photoemission processes. These methods fall into three broad categories: tailoring a material's optical absorption properties, improving carrier separation and transport, and modifying the material's crystal structure, morphology, or architecture. It is worth noting that over the last two decades, many semiconductor-based devices have benefited from systematic application of one or more of these methods to achieve record optical and electrical performance. For example, blue LEDs utilize GaN-based semiconductors with appropriate band-gap engineering, doping, and quantum-well structures to achieve $> 80\%$ efficiency for converting electrical current into optical output [119]. It is our assertion that utilizing such methods for developing the next generation of photocathodes should provide unique paths for simultaneously achieving new

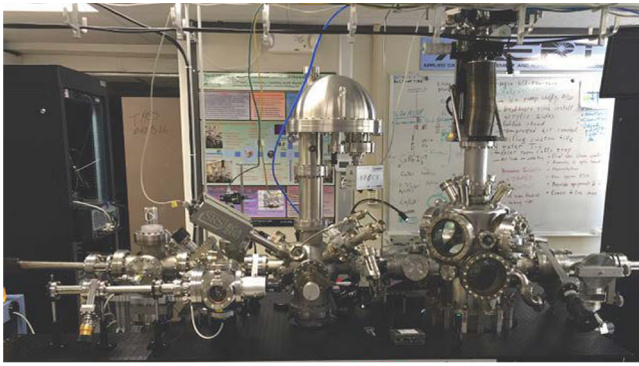


FIG. 17. Customized surface-science characterization system featuring *in situ* incorporation of x-ray photoemission spectroscopy (XPS), Auger spectroscopy, low-energy electron diffraction (LEED), and ion scattering spectroscopy (ISS) together with material synthesis and electron-beam measurement stations.

levels of quantum efficiency, low emittance, and longer lifetimes.

Photon absorption is a necessary first step in photoemission, and higher QEs are mostly attributable to the use of semiconductor materials having well-defined band gaps and relatively low electron affinities that promote electron emission into the vacuum. For ultra-fast photocathodes, work is underway to utilize wave-interference effects to modulate the absorption profile (e.g., absorption as a function of depth [33]) in a way that also enhances emission probability severalfold [120]. While largely theoretical in nature, early studies indicate experimental confirmation of these effects are likely. Compound III-V semiconductors (e.g., GaAs) and alkali antimonides are the most established photocathodes offering high QEs following appropriate surface treatments at the expense of limited lifetimes. With a focus on solar blind photocathodes, there has been limited success in developing wide bandgap III-V semiconductor-based photocathodes utilizing advanced nitride materials (e.g., GaN and AlN) as well as diamond and other exotic materials [121–124]. In some cases, QEs of well over 20% have been reported for NEA-treated GaN-based photocathodes under UV illumination. Various reports suggest that certain properties of GaN-based semiconductors can be tailored to enhance photoemission, including band-gap engineering [125,126], doping [127,128], utilizing inherent polarization fields [127], nanowire structures [129], quantum-well structures [125, 126], and heterojunction schemes [122,130]. Some of these reports show promising results for limited application areas, but systematic investigations are lacking and there is limited information regarding photocathode lifetimes and no information on emittance measurements.

With the established energetic neutral atom-beam lithography and epitaxy (ENABLE) nitride film growth capability [131–133] (see description below) [134],

systematic investigations of wide band-gap GaN-based photocathode candidates are possible. Of particular interest is utilizing the broad band-gap tunability of the Ga-In-N materials system [135] over a wide range of Ga-to-In compositions (band gap tunable from 3.4 eV for GaN to 0.7 eV for InN) to optimize the optical absorption of the material at energies just above the band gap for optimal QE and low emittance. Thus, the inherent advantages of indium gallium nitride materials ($\text{In}_x\text{Ga}_{1-x}\text{N}$, $0 \leq x \leq 1$), including tunable band gaps, chemical robustness, built-in electric fields, smooth surfaces, amenability to *n*- and *p*-type doping, and quantum-well confinement can be systematically optimized for overall photocathode performance [136]. In addition, wider band-gap nitride materials, such as AlN, $\text{Al}_x\text{Ga}_{1-x}\text{N}$, and $\text{Al}_x\text{In}_{1-x}\text{N}$ can be grown and incorporated into heterostructure architectures as appropriate for tailoring optimal photocathode performance.

Band-gap engineering involves tailoring the energy structure in a material through precisely controlled stoichiometry, including changes in band-gap energy as a function of depth in the material (e.g., graded band gaps). Graded band-gap architectures are of particular interest in photocathodes because such structures may provide another novel mechanism for influencing beam emittance that is not available in isotropic bulk materials. It should be possible to tailor the energy-gap profile to maximize forward transport and electron escape probability while minimizing the final energy distribution of emitted electrons. Thus, a means of directly minimizing electron-beam emittance is possible.

In general, depth-dependent energy-gap materials are sophisticated heterostructures that require low-temperature thin-film growth. For the broadly tunable wide band-gap semiconductor materials system InGaN, the unique ENABLE method uses an energetic beam of neutral nitrogen atoms with kinetic energies tunable from 1 to 5 eV as the active growth species to overcome reaction barriers, thereby eliminating the need for high substrate temperatures to activate desired surface chemistry [137]. The high kinetic energy and high reactivity of N atoms allows low-temperature, rapid growth of device quality GaN, InN, and InGaN films by simultaneously exposing substrates to energetic N atoms and an evaporated Ga and/or In metal flux [137,138] in a clean MBE environment.

The ability to reduce film growth temperatures using ENABLE is required for synthesis of graded band-gap materials [131] and most of the devices based on graded InGaN fall into the following categories: using graded InGaN as a buffer to alleviate strain in various InGaN based optoelectronic devices [139]; using graded InGaN as the active layer in quantum-well devices to take advantage of the band-gap bending and electric-field tailoring to enhance device performance [140]; and using graded InGaN as the active layer in photocathodes to take advantage of the inherent electric field for increasing

quantum efficiency [141]. Because the direct band gap of InGaN is tunable over a broad and relevant range of photon energies, this material and its synthesis procedures provide a unique system for studying tailored electronic band structures in photocathodes.

The following research priorities are suggested:

(a) *Near-term*: 1D quantum structures, heterostructures, and quantum-well nanostructures on metals and simple semiconductors, band bending in semiconductors

(b) *Long-term*: superlattices, discrete energy levels associated with resonant structures, quantum wells, 2D electron gases, and surface nanoengineered structures to filter and tune discrete E levels and tunneling and transport properties with differing impacts on QE, $\varepsilon_{n,rms}$, and Δt linkages

C. *In situ* surface-science characterization

A key requirement in utilizing the tools of surface science in photocathode studies is that they occur *in situ* (e.g., in the same pristine vacuum environment) as other functions such as material synthesis and beam physics measurements. Many techniques are used for materials chemical analysis and crystal structure measurements on photocathodes. X-ray diffraction (XRD) and low-energy electron diffraction (LEED) are used for crystal structure analysis. X-ray fluorescence (XRF), Auger spectroscopy, ion scattering spectroscopy (ISS) and x-ray photoemission spectroscopy (XPS) are used for chemical and stoichiometric information. For imaging and surface morphology, atomic force microscopy (AFM), x-ray reflectivity (XRR), and photoemission electron microscopy (PEEM) provide insight into film roughness and nonuniformity. These techniques allow the evaluation of material composition, crystal structure, electrical conductivity, surface morphology (roughness, lateral structure), layer thickness and the extent of interdiffusion, doping concentrations, and other relevant material properties. In some cases, additional insight can be obtained by making these measurements *in operando*—during the growth process

[142,143] allowing for adjusting growth parameters to account for material incorporation into the film during growth. A material-centric approach to photocathode development now requires the availability of some combination of such techniques. The realization of such a system is shown in Fig. 17.

Characterization of electrical and emission properties are critical for understanding photocathode performance. Other tools, such as angle-resolved photoemission spectroscopy (ARPES) and transverse momentum spread measurements are less common but need to be integrated into a material-centric approach to advanced photocathode development. Given that doping and band-structure engineering are becoming more prevalent, conductivity and related measurements (especially *in situ*) are increasingly desirable. Electron energy filtering techniques should benefit by using *in situ* photoluminescence to directly measure the peak energy of the filter.

These concepts suggest the following approaches:

(a) *Near-term*: evaluate material composition, crystal structure, surface morphology (roughness, lateral structure); layer thickness and extent of interdiffusion, doping concentration, and other relevant material properties

(b) *Long-term*: combine growth and analysis capabilities with the ability to introduce photocathodes into an accelerator and measure performance. Measurement capabilities to be emphasized include electronic and emission properties (conductivity, spectral response, transverse momentum spread, and temporal response). This goal will require significant standardization across the community and the adoption of best practices from adjacent disciplines (e.g., commercial semiconductor fabrication processes)

D. Correlation of beam properties and electronic band structure

Direct measurements establishing the correlation between electronic structure and its impact on the beam parameters,

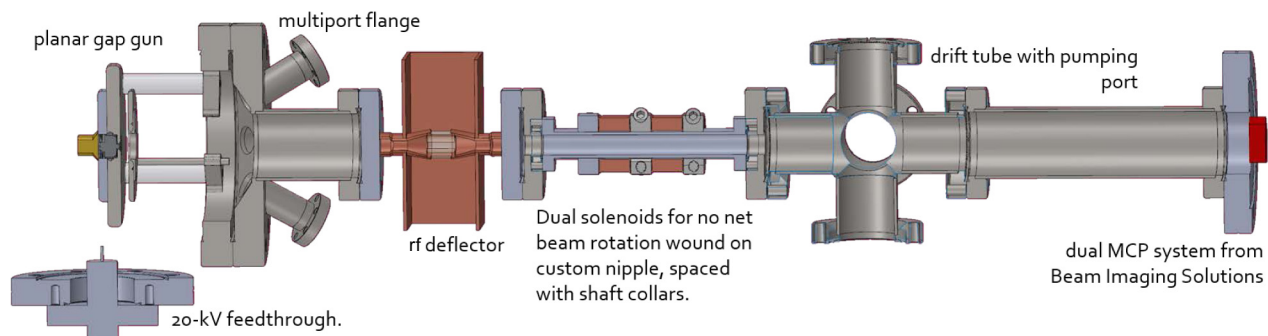


FIG. 18. Schematic showing key features of an integrated diagnostic for measurement of intrinsic energy spread, thermal emittance, longitudinal emittance, and emission promptness; based on the LBNL Momentatron [144].

particularly emittance and response time, are critical to the development of engineered quantum-confinement-based photoemitters. To date, most discussions of advanced cathodes have centered on reduction of the intrinsic energy spread, or thermal emittance, as this impacts the high-profile applications such as XFELs. However, other cathode properties, such as response time, or emission promptness, are also important. To this end, diagnostic systems, such as variations of the LBNL Momentatron [144] (see implementation in Fig. 18) and/or fully instrumented electron guns, must be used in conjunction with the previously discussed techniques to measure intrinsic energy spread, spectral response, and emission promptness as a function of material properties. Key practical features have begun to include sophisticated cathode insertion and translation mechanisms to allow *in situ* exchange of the cathode between synthesis and characterization stations, including photoinjectors. Figure 19 shows the latest iteration of LANL's adaptation to the LBNL/INFN photocathode geometry allowing compatible insertion and manipulation of the cathode with commercial surface-science characterization systems as well as photoinjectors.

The Momentatron works by accelerating photoemitted electrons across a gap and imaging the electron beam divergence on a phosphor screen detector situated a known distance from the cathode plane. Thermal emittance is then obtained via

$$\varepsilon_t = \frac{\varepsilon_{n,\text{rms}}}{\sigma_x} = r_s \left[\frac{q_e V}{3m_e c^2 (2g + L)^2} \right]^{1/2}, \quad (16)$$

where r_s is the spot size on the detector, and V is the accelerating voltage. Particle-tracking simulations of the

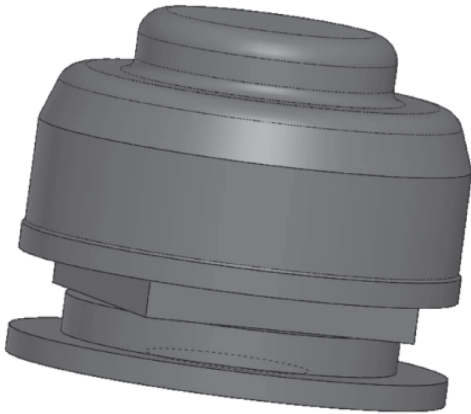


FIG. 19. Schematic of the modified LBNL/INFN interchangeable cathode geometry. The modifications are to accommodate (a) the insertion and manipulation of the cathode plug-in commercial surface-science characterization systems (that typically accept silicon wafer holders), and (b) the insertion of the cathode into a particular photoinjector.

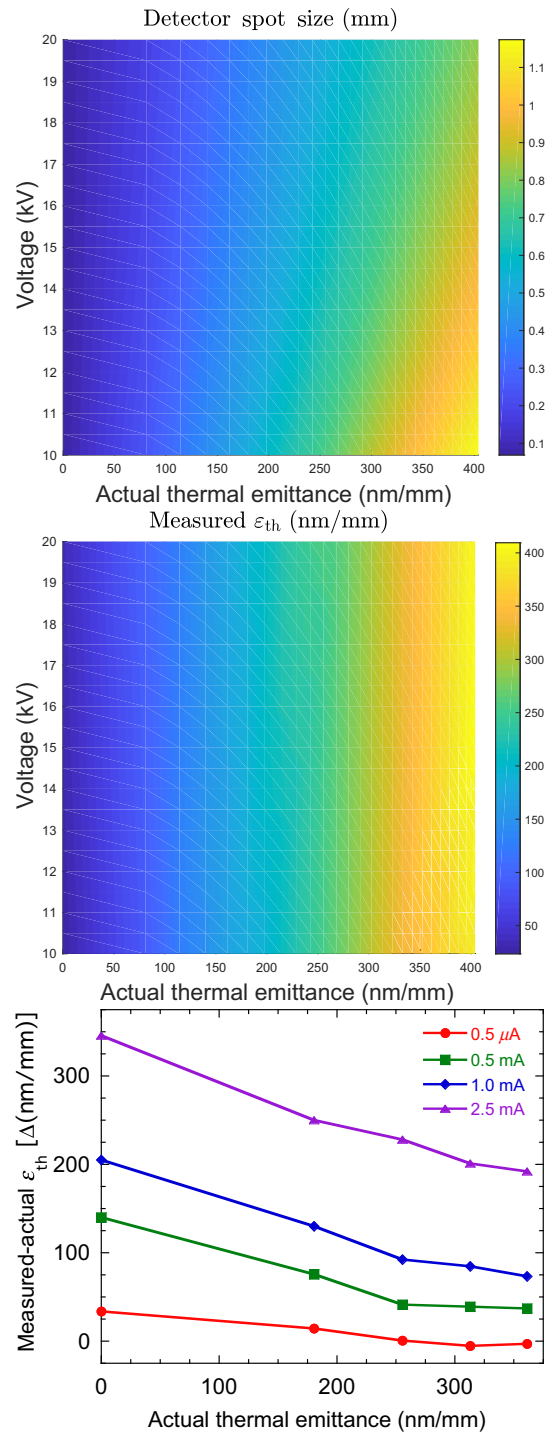


FIG. 20. Performance characteristics of a modified emittance measurement system based on the LBNL Momentatron [144]. *Top*: Detector spot size in mm (color) as a function of gap voltage and emittance shows that emittance values of interest correspond to spot sizes (from 0.2 to 1.0 mm) compatible with commercial multichannel plate (MCP) detectors; *Middle*: Read-out emittance in nm/mm (color) as a function of gap voltage and actual emittance, showing nearly uniform agreement for all ranges of operating voltage; *Bottom*: Measurement error as a function of actual thermal emittance at various beam currents.

Momentatron (e.g., 0.2-mm laser spot size, 2-ps emission time, and 20-kV accelerating voltage) indicate that measured thermal emittance is accurate down to 50 to 100 nm/mm for beam current on the order of 1 μ A, as shown in Fig. 20. In this study, the gap distance $g = 5$ mm and the drift length to detector is $L = 70$ cm. The transverse emittance measurement system is complemented by an integrated electron spectrometer, allowing investigations of asymmetry between transverse and longitudinal electron energy emission spectra. The cathode response time-measurement system accommodates a phase-locked laser and high-power rf source for finer resolution at lower bunch charges.

Not only must an engineered photocathode be thoroughly tested in a rf gun, but its properties must be sufficiently understood to enable simulation in an end-to-end beam code or a beam optics (particle-in-cell) simulation. Such a simulation will allow correlations between changes in the material's nanoscale properties to be observed in the resulting electron-beam performance. Characterization facilities such as those indicated in Fig. 17 are therefore integral to the effort. The following studies are suggested:

(a) *Near-term*: measure correlation between electronic structure and its impact on the beam parameters, particularly emittance; elucidate connection between specific design features of cathode (e.g., tailored nanostructures) and the resulting electron-beam properties

(b) *Long-term*: perform electron-beam simulations and beam physics measurements to show how material design features and changes in nanostructure impact electron-beam generation and properties

IV. CONCLUSIONS

In summary, a material-centric approach to understanding and exploiting nanostructure in photocathode films is outlined. The demands placed on photocathodes by challenging applications, in particular XFELs, are often conflicting with regards to (particularly) high quantum efficiency and low emittance, followed by bunch shape and lifetime. Given that improvements in one are often at the expense of another, there is a need to employ methods that undo their linkage. One path forward may be the use of quantum-dot-like structures, heterostructures, or introducing inhomogeneity at the nanoscale. Such a program requires theoretical support in addition to fabrication efforts. Perspectives regarding significant progress and remaining challenges are presented along with several potential paths forward, each drawing upon a requisite set of tools, methods, and instruments. Tailoring compositions and heterostructures in semiconductor photocathode films provides mechanisms for improving and tuning charge transport and photoemission. While these methods are still in their early stages of development,

they provide an optimistic future path towards overcoming the detrimental linkages identified in Sec. II that exist [most prominently, the joint increase of $\varepsilon_{n,rms}$ with QE as per Eq. (5)] amongst the identified photocathode metrics that prevent conventional bulk materials from meeting future demands. The potential benefits are roughly partitioned by:

(a) Modifications to the bulk materials properties: includes band bending or band-gap variation by doping or graded stoichiometries to create tailored conditions for photoabsorption (modification of the optical properties, particularly n and k) and photoexcitation (modification of the transport properties, particularly E_g , m_n). Such control can affect delayed emission by impacting photon absorption and electron transport;

(b) Energy filtering using nanostructure and surface structure: superlattices, discrete energy levels associated with resonant structures, quantum wells and dots, and 2D electron gases. Band bending in semiconductors likewise affects the photoemission process (as well as field emission [145]). Surface nanoengineered filter structures can affect discrete energy levels, tunneling and transport properties, and potentially separate the linkages between QE, $\varepsilon_{n,rms}$, and response time.

Unlike conventional bulk and surface semiconductors, nanostructures and compositional variations provide multiple approaches for improving photon absorption and electron emission. Two-dimensional layers, such as graphene, boron-nitride, etc., may further provide a protective layer for the photocathode surface. Instead of local conditions governing the transport and emission probabilities, heterostructures and nanocrystalline materials may yield conditions where photoemission is dictated by electron wave functions being extended over many adjacent structures. This suggests techniques to improve forward electron transport and quantum efficiency may be employed without significant effect on transverse energy and emittance. Moreover, a means to control the spread in energy emerges whereby heterostructures can potentially act as an electron source or as an energy filter to modulate transport past the surface.

The overarching goal in developing heterostructures and nanoengineered materials is to favor electron transport in the direction of the surface normal while maintaining high quantum efficiency. Doing so, without significantly increasing emittance in the transverse direction, will be a noteworthy and technologically enabling accomplishment.

ACKNOWLEDGMENTS

This work is supported by the Laboratory Directed Research and Development program of Los Alamos National Laboratory under project No. 20150394DR. Los

Alamos National Laboratory is operated by Los Alamos National Security, LLC, for the National Nuclear Security Administration of the U.S. Department of Energy (Contract No. DE-AC52-06NA25396). We thank B. Carlsten and R. Sheffield (LANL) for helpful discussions and critical review as well as H. Padmore (LBNL) and T. Vecchione (SLAC) for experimental advice. We thank D. Dalmas, F. Romero, and B. Romero (LANL) for their support on many technical aspects of the LANL experiments and R. Hand (Hand Precision Machining) for his timely support on complex fabrication. Lastly, we thank J. J. Petillo for discussions regarding particle-in-cell and beam optics codes.

Note added.—Recently, a manuscript treating the decoupling of the correlation between QE and emittance for single-crystal photocathodes appeared after submission of the present work, and is Karkare *et al.* (2017) *Phys. Rev. Lett.* **118**, 164802.

-
- [1] B. McNeil, Free electron lasers: First light from hard X-ray laser, *Nat. Photonics* **3**, 375 (2009).
- [2] S. Jamison, X-ray science: X-ray FEL shines brightly, *Nat. Photonics* **4**, 589 (2010).
- [3] I. Schlichting, Serial femtosecond crystallography: The first five years, *IUCrJ* **2**, 246 (2015).
- [4] P. Emma, R. Akre, J. Arthur, R. Bionta, C. Bostedt, J. Bozek, A. Brachmann, P. Bucksbaum, R. Coffee, F.-J. Decker, Y. Ding, D. Dowell, S. Edstrom, A. Fisher, J. Frisch, S. Gilevich, J. Hastings, G. Hays, P. Hering, Z. Huang, R. Iverson, H. Loos, M. Messerschmidt, A. Miahnahri, S. Moeller, H.-D. Nuhn, G. Pile, D. Ratner, J. Rzepiela, D. Schultz, T. Smith, P. Stefan, H. Tompkins, J. Turner, J. Welch, W. White, J. Wu, G. Yocky, and J. Galayda, First lasing and operation of an ångström-wavelength free-electron laser, *Nat. Photonics* **4**, 641 (2010).
- [5] G. R. Fleming and M. A. Ratner, Grand challenges in basic energy sciences, *Phys. Today* **61**, 28 (2008).
- [6] D. H. Dowell, I. Bazarov, B. Dunham, K. Harkay, C. Hernandez-Garcia, R. Legg, H. Padmore, T. Rao, J. Smedley, and W. Wan, Cathode R&D for future light sources, *Nucl. Instrum. Methods Phys. Res. Sect. A* **622**, 685 (2010).
- [7] T. C. Katsouleas, R. Alarcon, J. Albertine, I. Ben-Zvi, S. G. Biedron, C. Brau, W. B. Colson, R. C. Davidson, P. G. Gaffney II, L. Merminga, J. D. Miller, B. E. Newnam, P. G. O’Shea, C. K. N. Patel, D. Prosnitz, and E. Zimet, *Scientific Assessment of High-Power Free-Electron Laser Technology* (National Academies Press, Washington, DC, 2009).
- [8] C. Pellegrini, Progress toward a soft x-ray FEL, *Nucl. Instrum. Methods Phys. Res. Sect. A* **272**, 364 (1988).
- [9] P. G. O’Shea and H. P. Freund, Laser technology – free-electron lasers: Status and applications, *Science* **292**, 1853 (2001).
- [10] D. H. Dowell and J. F. Schmerge, Quantum efficiency and thermal emittance of metal photocathodes, *Phys. Rev. Spec. Top. Accel. Beams* **12**, 074201 (2009).
- [11] I. V. Bazarov, D. G. Ouzounov, B. M. Dunham, S. A. Belomestnykh, Y. Li, X. Liu, R. E. Meller, J. Sikora, C. K. Sinclair, F. W. Wise, and T. Miyajima, Efficient temporal shaping of electron distributions for high-brightness photoemission electron guns, *Phys. Rev. Spec. Top. Accel. Beams* **11**, 040702 (2008).
- [12] K. L. Jensen, J. J. Petillo, S. Ovtchinnikov, D. N. Panagos, N. A. Moody, and S. G. Lambrakos, Modeling emission lag after photoexcitation, *J. Appl. Phys.* **122**, 164501 (2017).
- [13] D. Dowell, K. Davis, K. Friddell, E. Tyson, C. Lancaster, L. Milliman, R. Rodenburg, T. Aas, M. Bemes, S. Bethel, P. Johnson, K. Murphy, C. Whelen, J. Adamski, D. Pioresi, D. Shoffstall, G. Busch, and D. Remelius, in *Particle Accelerator Conference, 1993* (Washington, DC, 1993), Vol. 4, p. 2967.
- [14] D. H. Dowell, S. Z. Bethel, and K. D. Friddell, Results from the average power laser experiment photocathode injector test, *Nucl. Instrum. Methods Phys. Res. Sect. A* **356**, 167 (1995).
- [15] K. L. Jensen, D. W. Feldman, N. A. Moody, and P. G. O’Shea, A photoemission model for low work function coated metal surfaces and its experimental validation, *J. Appl. Phys.* **99**, 124905 (2006).
- [16] K. L. Jensen, General formulation of thermal, field, and photoinduced electron emission, *J. Appl. Phys.* **102**, 024911 (2007).
- [17] K. L. Jensen, P. G. O’Shea, and D. W. Feldman, Emittance of a photocathode: Effects of temperature and field, *Phys. Rev. Spec. Top. Accel. Beams* **13**, 080704 (2010).
- [18] S. H. Kong, J. Kinross-Wright, D. C. Nguyen, and R. L. Sheffield, Photocathodes for free electron lasers, *Nucl. Instrum. Methods Phys. Res. Sect. A* **358**, 272 (1995).
- [19] N. A. Moody, K. L. Jensen, D. W. Feldman, P. G. O’Shea, and E. J. Montgomery, Prototype dispenser photocathode: Demonstration and comparison to theory, *Appl. Phys. Lett.* **90**, 114108 (2007).
- [20] N. A. Moody, K. L. Jensen, D. W. Feldman, E. J. Montgomery, and P. G. O’Shea, Factors affecting performance of dispenser photocathodes, *J. Appl. Phys.* **102**, 104901 (2007).
- [21] B. M. van Oerle and G. J. Ernst, On the use of CsK₂Sb photocathodes in RF linacs, *Nucl. Instrum. Methods Phys. Res. Sect. A* **358**, 287 (1995).
- [22] B. Dunham, J. Barley, A. Bartnik, I. Bazarov, L. Cultrera, J. Dobbins, G. Hoffstaetter, B. Johnson, R. Kaplan, S. Karkare, V. Kostroun, Y. Li, M. Liepe, X. Liu, F. Loehl, J. Maxson, P. Quigley, J. Reilly, D. Rice, D. Sabol, E. Smith, K. Smolenski, M. Tigner, V. Vesherevich, D. Widger, and Z. Zhao, Record high-average current from a high-brightness photoinjector, *Appl. Phys. Lett.* **102**, 034105 (2013).
- [23] K. L. Jensen, N. A. Moody, D. W. Feldman, E. J. Montgomery, and P. G. O’Shea, Photoemission from metals and cesiated surfaces, *J. Appl. Phys.* **102**, 074902 (2007).
- [24] K. L. Jensen, B. Jensen, E. J. Montgomery, D. W. Feldman, P. G. O’Shea, and N. A. Moody, Theory of photoemission from cesium antimonide using an

- alpha-semiconductor model, *J. Appl. Phys.* **104**, 044907 (2008).
- [25] L. Cultrera, I. Bazarov, A. Bartnik, B. Dunham, S. Karkare, R. Merluzzi, and M. Nichols, Thermal emittance and response time of a cesium antimonide photocathode, *Appl. Phys. Lett.* **99**, 152110 (2011).
- [26] I. V. Bazarov, B. M. Dunham, X. Liu, M. Virgo, A. M. Dabiran, F. Hannon, and H. Sayed, Thermal emittance and response time measurements of a GaN photocathode, *J. Appl. Phys.* **105**, 08375 (2009).
- [27] S. Karkare and I. Bazarov, Effect of nanoscale surface roughness on transverse energy spread from GaAs photocathodes, *Appl. Phys. Lett.* **98**, 094104 (2011).
- [28] J. Feng, S. Karkare, J. Nasiatka, S. Schubert, J. Smedley, and H. Padmore, Near atomically smooth alkali antimonide photocathode thin films, *J. Appl. Phys.* **121**, 044904 (2017).
- [29] Disorder-induced heating is due to Coulomb interactions in the emitted beam: although their focus is on emitters without nano or microscale structures, Maxson, *et al.* [146] implicitly suggest heterostructures may have benefit.
- [30] L. Cultrera, S. Karkare, H. Lee, X. Liu, I. Bazarov, and B. Dunham, Cold electron beams from cryocooled, alkali antimonide photocathodes, *Phys. Rev. Spec. Top. Accel. Beams* **18**, 113401 (2015).
- [31] T. Vecchione, J. Feng, W. Wan, H. A. Padmore, I. Ben-Zvi, X. Liang, M. Ruiz-Oses, T. Rao, J. Smedley, and D. Dowell, in *International Particle Accelerator Conference* (New Orleans, LA, 2012).
- [32] R. Xiang and J. Teichert, Photocathodes for high brightness photo injectors, *Phys. Procedia* **77**, 58 (2015).
- [33] J. Smedley, M. Gaowei, J. Sinsheimer, K. Attenkfer, J. Walsh, S. Schubert, J. Wong, H. Padmore, J. Kuhn, E. Muller, Z. Ding, H. Frisch, H. B. Bhandari, H. Lingertat, V. Wang, O. Ovechkina, and V. V. Nagarkar, *Proceedings of IPAC 2015 Sputter Growth of Alkali Antimonide Photocathodes: An in Operando Materials Analysis, Richmond, VA, 2015* (IPAC 2015, Richmond, VA, 2015).
- [34] We thank an anonymous reviewer for pointing out the relation of what is advocated here to an earlier work: Nemeth *et al.* (2010) *Phys. Rev. Lett.* **104** 046801.
- [35] K. L. Jensen, E. W. Montgomery, D. W. Feldman, P. G. O'Shea, J. R. Harris, J. W. Lewellen, and N. A. Moody, Multiple scattering effects on quantum efficiency and response time for cesiated metal photocathodes, *J. Appl. Phys.* **110**, 034504 (2011).
- [36] C. N. Berglund and W. E. Spicer, I – photoemission studies of copper and silver: Theory, *Phys. Rev.* **136**, A1030 (1964).
- [37] W. F. Krolikowski and W. E. Spicer, Photoemission studies of the noble metals. I. Copper, *Phys. Rev.* **185**, 882 (1969).
- [38] W. E. Spicer and A. Herrera-Gomez, Modern theory and applications of photocathodes, *Proc. SPIE* **2022**, 18 (1993).
- [39] J. W. Lewellen, in *Proceedings of the IEEE Particle Accelerator Conference, Knoxville, TN, 2005* (IEEE PAC, Knoxville, TN, 2005), p. 563.
- [40] A. di Bona, F. Sabary, S. Joly, P. Michelato, D. Sertore, C. Pagani, and S. Valeri, Development, operation and analysis of bi-alkali antimonide photocathodes for high-brightness photo-injectors, *Nucl. Instrum. Methods Phys. Res. Sect. A* **385**, 385 (1997).
- [41] P. Michelato, Photocathodes for RF photoinjectors, *Nucl. Instrum. Methods Phys. Res. Sect. A* **393**, 455 (1997).
- [42] K. L. Jensen, D. A. Shiffler, J. J. Petillo, Z. Pan, and J. W. Luginsland, Emittance, surface structure, and electron emission, *Phys. Rev. Spec. Top. Accel. Beams* **17**, 043402 (2014).
- [43] T. Vecchione, J. Feng, W. Wan, H. A. Padmore, I. Ben-Zvi, X. Liang, M. Ruiz-Oses, T. Rao, J. Smedley, and D. Dowell, *Effect of Roughness on Emittance of Potassium Cesium Antimonide Photocathodes* (IEEE, New Orleans, LA, 2012).
- [44] D. H. Dowell, Sources of Emittance in RF Photocathode Injectors: Intrinsic emittance, space charge forces due to non-uniformities, RF and solenoid effects, arXiv:1610.01242v3 (2016).
- [45] A. H. Sommer, Stability of photocathodes, *Appl. Opt.* **12**, 90 (1973).
- [46] C. Y. Su, P. W. Chye, P. Pianetta, I. Lindau, and W. E. Spicer, Oxygen adsorption on Cs covered GaAs(110) surfaces, *Surf. Sci.* **86**, 894 (1979).
- [47] M. Kamaratos, Adsorption kinetics of the Cs-O activation layer on GaAs(1 0 0), *Appl. Surf. Sci.* **185**, 66 (2001).
- [48] N. Chanlek, J. D. Herbert, R. M. Jones, L. B. Jones, K. J. Middleman, and B. L. Militsyn, The degradation of quantum efficiency in negative electron affinity GaAs photocathodes under gas exposure, *J. Phys. D* **47**, 055110 (2014).
- [49] V. Pavlenko, F. Liu, M. A. Hoffbauer, N. A. Moody, and E. R. Batista, Kinetics of alkali-based photocathode degradation, *AIP Adv.* **6**, 115008 (2016).
- [50] G. Wang, R. Pandey, N. A. Moody, and E. R. Batista, Degradation of alkali-based photocathodes from exposure to residual gases: A first-principles study, *J. Phys. Chem. C* **121**, 8399 (2017).
- [51] A. H. Sommer, *Photoemissive Materials: Preparation, Properties, and Uses* (Wiley, New York, 1968).
- [52] M. Xie, Exact and variational solutions of 3D eigenmodes in high gain FELs, *Nucl. Instrum. Methods Phys. Res. Sect. A* **445**, 59 (2000).
- [53] G. Marcus, E. Hemsing, and J. Rosenzweig, Gain length fitting formula for free-electron lasers with strong space-charge effects, *Phys. Rev. Spec. Top. Accel. Beams* **14**, 080702 (2011).
- [54] J. Smedley, T. Rao, and D. A. Dimitrov, *An Engineering Guide to Photoinjectors Photocathode Theory* (CreateSpace Independent Publishing Platform, 2016).
- [55] S. V. Milton, E. Gluskin, N. D. Arnold, C. Benson, W. Berg, S. G. Biedron, M. Borland, Y.-C. Chae, R. J. Dejus, P. K. Den Hartog, B. Deriy, M. Erdmann, Y. I. Eidelman, M. W. Hahne, Z. Huang, K.-J. Kim, J. W. Lewellen, Y. Li, A. H. Lumpkin, O. Makarov, E. R. Moog, A. Nassiri, V. Sajaev, R. Soliday, B. J. Tieman, E. M. Trakhtenberg, G. Travish, I. B. Vasserman, N. A. Vinokurov, X. J. Wang, G. Wiemerslage, and B. X. Yang, Exponential gain and saturation of a self-amplified spontaneous emission free-electron laser, *Science* **292**, 2037–2041 (2001).
- [56] J. W. Lewellen, in *Photocathode Physics for Photoinjectors (P3) Workshop, Newport News, VA, 2016*.

- [57] M. Krasilnikov, F. Stephan, G. Asova, H.-J. Grabosch, M. Groß, L. Hakobyan, I. Isaev, Y. Ivanisenko, L. Jachmann, M. Khojoyan, G. Klemz, W. Köhler, M. Mahgoub, D. Maljutin, M. Nozdrin, A. Oppelt, M. Otevrel, B. Petrosyan, S. Rimjaem, A. Shapovalov, G. Vashchenko, S. Weidinger, R. Wennendorff, K. Flöttmann, M. Hoffmann, S. Lederer, H. Schlarb, S. Schreiber, I. Templin, I. Will, V. Paramonov, and D. Richter, Experimentally minimized beam emittance from an *L*-band photoinjector, *Phys. Rev. Spec. Top. Accel. Beams* **15**, 100701 (2012).
- [58] W. E. Spicer, Photoemissive, photoconductive, and optical absorption studies of alkali-antimony compounds, *Phys. Rev.* **112**, 114 (1958).
- [59] D. H. Dowell, F. K. King, R. E. Kirby, J. F. Schmerge, and J. M. Smedley, *In situ* cleaning of metal cathodes using a hydrogen ion beam, *Phys. Rev. Spec. Top. Accel. Beams* **9**, 063502 (2006).
- [60] K. L. Jensen, Scattering and the relationship between quantum efficiency and emittance, *J. Appl. Phys.* **113**, 056101 (2013).
- [61] K. L. Jensen, J. J. Petillo, D. N. Panagos, S. Ovtchinnikov, and N. A. Moody, Delayed photo-emission model for beam optics codes, *J. Vac. Sci. Technol. B* **35**, 02C102 (2017).
- [62] D. G. Fisher, R. E. Enstrom, J. S. Escher, and B. F. Williams, Photoelectron surface escape probability of (Ga,In)As : Cs-O in the 0.9 to $\sim 1.6 \mu\text{m}$ range, *J. Appl. Phys.* **43**, 3815 (1972).
- [63] R. H. Fowler and L. Nordheim, Electron emission in intense electric fields, *Proc. R. Soc. London, Sect. A* **119**, 173 (1928).
- [64] K. L. Jensen, D. Finkenstadt, A. Shabaev, S. G. Lambrakos, N. A. Moody, J. J. Petillo, H. Yamaguchi, and F. Liu, A photoemission moments model using density functional and transfer matrix methods applied to coating layers on surfaces: Theory, *J. Appl. Phys.* **123**, 045301 (2018).
- [65] K. L. Jensen, *Electron Emission Physics* (Academic Press, San Diego, CA, 2007).
- [66] E. A. Taft and H. R. Philipp, Structure in the energy distribution of photoelectrons from K3Sb and Cs3Sb, *Phys. Rev.* **115**, 1583 (1959).
- [67] I. Bazarov, L. Cultrera, A. Bartnik, B. Dunham, S. Karkare, Y. Li, X. Liu, J. Maxson, and W. Roussel, Thermal emittance measurements of a cesium potassium antimonide photocathode, *Appl. Phys. Lett.* **98**, 083715 (2011).
- [68] P. Michelato, P. Gallina, and C. Pagani, Alkali photocathode development for superconducting rf guns, *Nucl. Instrum. Methods Phys. Res. Sect. A* **340**, 176 (1994).
- [69] K. L. Jensen, A tutorial on electron sources, *IEEE Trans. Plasma Sci.* **46**, 1881 (2018).
- [70] D. W. Feldman, S. C. Bender, B. Carlsten, J. Early, R. B. Feldman, W. J. D. Johnson, A. Lumpkin, P. G. O'Shea, W. E. Stein, R. L. Sheffield, and K. McKenna, Performance of the Los Alamos HIBAF Accelerator At 17 Mev, *Nucl. Instrum. Methods Phys. Res. Sect. A* **304**, 224 (1991).
- [71] H. Yamaguchi, F. Liu, J. DeFazio, C. W. Narvaez Villarrubia, D. Finkenstadt, A. Shabaev, K. L. Jensen, V. Pavlenko, M. Mehl, S. Lambrakos, G. Gupta, A. D. Mohite, N. A. Moody, and J. Smedley, Active bialkali photocathodes on free-standing graphene substrates photocathode physics for photoinjectors (P3) workshop overview of photocathode physics, *npj 2D Mater. Appl.* **1**, 12 (2017).
- [72] K. L. Jensen, A quantum dipole-modified work function for a simplified electron emission barrier, *J. Appl. Phys.* **111**, 054916 (2012).
- [73] C. R. Kagan and C. B. Murray, Charge transport in strongly coupled quantum dot solids, *Nat. Nanotechnol.* **10**, 1013 (2015).
- [74] A. Shabaev, A. L. Efros, and A. L. Efros, Dark and photoconductivity in ordered array of nanocrystals, *Nano Lett.* **13**, 5454 (2013).
- [75] B. H. Savitzky, R. Hovden, K. Whitham, J. Yang, F. Wise, T. Hanrath, and L. F. Kourkoutis, Propagation of structural disorder in epitaxially connected quantum dot solids from atomic to micron scale, *Nano Lett.* **16**, 5714 (2016).
- [76] M. A. Boles and D. V. Talapin, Self-assembly of tetrahedral CdSe nanocrystals: Effective "Patchiness" via anisotropic steric interaction, *J. Am. Chem. Soc.* **136**, 5868 (2014).
- [77] J. Maxson, P. Musumeci, L. Cultrera, S. Karkare, and H. Padmore, Ultrafast laser pulse heating of metallic photocathodes and its contribution to intrinsic emittance, *Nucl. Instrum. Methods Phys. Res. Sect. A* **865**, 99 (2017).
- [78] N. A. Moody, *Photocathode Physics for Photoinjectors (P3) Workshop LANL Updates and Quantum Dots: Photoemission from Quantized Energy States*, Newport News, VA, 2016.
- [79] E. Oh, A. L. Huston, A. Shabaev, A. Efros, M. Currie, K. Susumu, K. Bussmann, R. Goswami, F. K. Fatemi, and I. L. Medintz, Energy transfer sensitization of luminescent gold nanoclusters: More than just the classical forster mechanism, *Sci. Rep.* **6**, 35538 (2016).
- [80] K. L. Jensen, D. A. Shiffler, I. M. Rittersdorf, J. L. Lebowitz, J. R. Harris, Y. Y. Lau, J. J. Petillo, W. Tang, and J. W. Luginsland, Discrete space charge affected field emission: Flat and hemisphere emitters, *J. Appl. Phys.* **117**, 194902 (2015).
- [81] P. Deak, T. Frauenheim, and M. R. Pederson, *Computer Simulation of Materials at Atomic Level* (Wiley-VCH Verlag GmbH & Co. KGaA, Berlin, Germany, 2005).
- [82] W. K. Bae, L. A. Padilha, Y.-S. Park, H. McDaniel, I. Robel, J. M. Pietryga, and V. I. Klimov, Controlled alloying of the core-shell interface in CdSe/CdS quantum dots for suppression of Auger recombination, *ACS Nano* **7**, 3411 (2013).
- [83] L. E. Brus, A simple model for the ionization potential, electron affinity, and aqueous redox potentials of small semiconductor crystallites, *J. Chem. Phys.* **79**, 5566 (1983).
- [84] A. I. Ekimov, A. L. Efros, and A. A. Onushchenko, Quantum size effect in semiconductor microcrystals, *Solid State Commun.* **56**, 921 (1985).
- [85] J. M. Pietryga, K. K. Zhuravlev, M. Whitehead, V. I. Klimov, and R. D. Schaller, Evidence for Barrierless Auger Recombination in PbSe Nanocrystals: A Pressure-Dependent Study of Transient Optical Absorption, *Phys. Rev. Lett.* **101**, 217401 (2008).
- [86] J. M. Pietryga, Y.-S. Park, J. Lim, A. F. Fidler, W. K. Bae, S. Brovelli, and V. I. Klimov, Spectroscopic and device

- aspects of nanocrystal quantum dots, *Chem. Rev.* **116**, 10513 (2016).
- [87] N. S. Makarov, J. Lim, Q. Lin, J. W. Lewellen, N. A. Moody, I. Robel, and J. M. Pietryga, Quantum dot thin-films as rugged, high-performance photocathodes, *Nano Lett.* **17**, 2319 (2017).
- [88] H. Zang, H. Li, N. S. Makarov, K. A. Velizhanin, K. Wu, Y.-S. Park, and V. I. Klimov, Thick-shell CuInS₂/ZnS quantum dots with suppressed blinking and narrow single-particle emission line widths, *Nano Lett.* **17**, 1787 (2017).
- [89] F. Fan, O. Voznyy, R. P. Sabatini, K. T. Bicanic, M. M. Adachi, J. R. McBride, K. R. Reid, Y.-S. Park, X. Li, A. Jain, R. Quintero-Bermudez, M. Saravanapavanantham, M. Liu, M. Korkusinski, P. Hawrylak, V. I. Klimov, S. J. Rosenthal, S. Hoogland, and E. H. Sargent, Continuous-wave lasing in colloidal quantum dot solids enabled by facet-selective epitaxy, *Nature* **544**, 75 (2017).
- [90] P. Dolizy and F. Groliere, Dissociation-energies of alkali antimonides as thin-layers, *J. Phys. D* **19**, 687 (1986).
- [91] V. L. Colvin, A. P. Alivisatos, and J. G. Tobin, Valence-Band Photoemission from a Quantum-Dot System, *Phys. Rev. Lett.* **66**, 2786 (1991).
- [92] A. M. Munro, B. Zacher, A. Graham, and N. R. Armstrong, Photoemission spectroscopy of tethered CdSe nanocrystals: Shifts in ionization potential and local vacuum level as a function of nanocrystal capping ligand, *ACS Appl. Mater. Interfaces* **2**, 863 (2010).
- [93] D. V. Talapin and C. B. Murray, PbSe nanocrystal solids for n- and p-channel thin film field-effect transistors, *Science* **310**, 86 (2005).
- [94] M. V. Kovalenko, M. Scheele, and D. V. Talapin, Colloidal nanocrystals with molecular metal chalcogenide surface ligands, *Science* **324**, 1417 (2009).
- [95] Y. Liu, M. Gibbs, C. L. Perkins, J. Tolentino, M. H. Zarghami, J. Bustamante, and M. Law, Robust, functional nanocrystal solids by infilling with atomic layer deposition, *Nano Lett.* **11**, 5349 (2011).
- [96] Y. Liu, J. Tolentino, M. Gibbs, R. Ihly, C. L. Perkins, Y. Liu, N. Crawford, J. C. Hemminger, and M. Law, PbSe quantum dot field-effect transistors with air-stable electron mobilities above 7 cm²/Vs, *Nano Lett.* **13**, 1578 (2013).
- [97] T.-H. Kim, K.-S. Cho, E. K. Lee, S. J. Lee, J. Chae, J. W. Kim, D. H. Kim, J.-Y. Kwon, G. Amaratunga, S. Y. Lee, B. L. Choi, Y. Kuk, J. M. Kim, and K. Kim, Full-colour quantum dot displays fabricated by transfer printing, *Nat. Photonics* **5**, 176 (2011).
- [98] H. McDaniel, N. Fuke, N. S. Makarov, J. M. Pietryga, and V. I. Klimov, An integrated approach to realizing high-performance liquid-junction quantum dot sensitized solar cells, *Nat. Commun.* **4**, 2887 (2013).
- [99] O. E. Semonin, J. M. Luther, S. Choi, H.-Y. Chen, J. Gao, A. J. Nozik, and M. C. Beard, Peak external photocurrent quantum efficiency exceeding 100 percent via MEG in a quantum dot solar cell, *Science* **334**, 1530 (2011).
- [100] W. K. Bae, Y.-S. Park, J. Lim, D. Lee, L. A. Padilha, H. McDaniel, I. Robel, C. Lee, J. M. Pietryga, and V. I. Klimov, Controlling the influence of Auger recombination on the performance of quantum-dot light-emitting diodes, *Nat. Commun.* **4**, 2661 (2013).
- [101] J. M. Caruge, J. E. Halpert, V. Wood, V. Bulovic, and M. G. Bawendi, Colloidal quantum-dot light-emitting diodes with metal-oxide charge transport layers, *Nat. Photonics* **2**, 247 (2008).
- [102] G. Konstantatos, I. Howard, A. Fischer, S. Hoogland, J. Clifford, E. Klem, L. Levina, and E. H. Sargent, Ultrasensitive solution-cast quantum dot photodetectors, *Nature* **442**, 180 (2006).
- [103] B. N. Pal, I. Robel, A. Mohite, R. Laocharoensuk, D. J. Werder, and V. I. Klimov, High-sensitivity *p* – *n* junction photodiodes based on PbS nanocrystal quantum dots, *Adv. Funct. Mater.* **22**, 1741 (2012).
- [104] J. M. Luther, J. Gao, M. T. Lloyd, O. E. Semonin, M. C. Beard, and A. J. Nozik, Stability assessment on a 3 percent bilayer PbS/ZnO quantum dot heterojunction solar cell, *Adv. Mater.* **22**, 3704 (2010).
- [105] C.-H. M. Chuang, P. R. Brown, V. Bulovic, and M. G. Bawendi, Improved performance and stability in quantum dot solar cells through band alignment engineering, *Nat. Mater.* **13**, 796 (2014).
- [106] X. Lan, O. Voznyy, F. P. García de Arquer, M. Liu, J. Xu, A. H. Proppe, G. Walters, F. Fan, H. Tan, M. Liu, Z. Yang, S. Hoogland, and E. H. Sargent, 10.6% certified colloidal quantum dot solar cells via solvent-polarity-engineered halide passivation, *Nano Lett.* **16**, 4630 (2016).
- [107] O. Sublemontier, C. Nicolas, D. Aureau, M. Patanen, H. Kintz, X. Liu, M.-A. Gaveau, J.-L. Le Garrec, E. Robert, F.-A. Barreda, A. Etcheberry, C. Reynaud, J. B. Mitchell, and C. Miron, X-ray photoelectron spectroscopy of isolated nanoparticles, *J. Phys. Chem. Lett.* **5**, 3399 (2014).
- [108] S. Schubert, M. Ruiz-Oses, I. Ben-Zvi, T. Kamps, X. Liang, E. Muller, K. Mueller, H. Padmore, T. Rao, X. Tong, T. Vecchione, and J. Smedley, Bi-alkali antimonide photocathodes for high brightness accelerators, *APL Mater.* **1**, 032119 (2013).
- [109] T. Vecchione, I. Ben-Zvi, D. H. Dowell, J. Feng, T. Rao, J. Smedley, W. Wan, and H. A. Padmore, A low emittance and high efficiency visible light photocathode for high brightness accelerator-based x-ray light sources, *Appl. Phys. Lett.* **99**, 034103 (2011).
- [110] T. Wada, T. Nitta, T. Nomura, M. Miyao, and M. Hagino, Influence of exposure to CO, CO₂ and H₂O on the stability of GaAs photocathodes, *Jpn. J. Appl. Phys.* **29**, 2087 (1990).
- [111] See <http://www-public.slac.stanford.edu/sciDoc/docMeta.aspx?slacPubNumber=SLAC-PUB-15321>.
- [112] G. Wang, P. Yang, N. A. Moody, and E. R. Batista, Overcoming the quantum efficiency-lifetime tradeoff of photocathodes by coating with atomically thin two-dimensional nanomaterials, *npj 2D Mater. Appl.* **2**, 17 (2018).
- [113] F. Liu, N. A. Moody, K. L. Jensen, V. Pavlenko, C. W. Narvaez Villarrubia, A. D. Mohite, and G. Gupta, Single layer graphene protective gas barrier for copper photocathodes, *Appl. Phys. Lett.* **110**, 041607 (2017).
- [114] N. A. Moody, H. Yamaguchi, G. Gupta, and A. D. Mohite, Graphene shield-enhancement of photosensitive surfaces and devices, *Proc. SPIE Micro- Nanotechnol. Sensors Syst. Appl.* **VI 9083**, 908333–909083 (2014).
- [115] H. Yamaguchi, F. Liu, J. DeFazio, M. Gaowei, C. W. Narvaez, J. Xie, J. Sinsheimer, D. Strom, V. Pavlenko, K. L. Jensen, J. Smedley, A. D. Mohite, and N. A. Moody, Photocathode: Free-standing bialkali photocathodes using

- atomically thin substrates, *Adv. Mater. Interfaces* **5**, 1870065 (2018).
- [116] V. Sverdlov, E. Ungersboeck, H. Kosina, and S. Selberherr, Current transport models for nanoscale semiconductor devices, *Mater. Sci. Eng. R* **58**, 228 (2008).
- [117] K. F. Brennan and C. Summers, Theory of resonant tunneling in a variably spaced multi-quantum well structure – an airy function-approach, *J. Appl. Phys.* **61**, 614 (1987).
- [118] K. L. Jensen, On the application of quantum transport theory to electron sources, *Ultramicroscopy* **95**, 29 (2003).
- [119] P. Pust, P. J. Schmidt, and W. Schnick, A revolution in lighting, *Nat. Mater.* **14**, 454 (2015).
- [120] A. Alexander, N. A. Moody, P. R. Bandaru, and J. M. Smedley, Enhanced photocathode performance through optimization of film thickness and substrate US Particle Accelerator School (USPAS) Lecture 2: Cathode Theory, *J. Vac. Sci. Technol. B* **35**, 022202 (2017).
- [121] O. H. W. Siegmund, A. S. Tremsin, J. V. Vallerga, J. B. McPhate, J. S. Hull, J. Malloy, and A. M. Dabiran, Gallium nitride photocathode development for imaging detectors, *Proc. SPIE* **7021**, 70211B (2008).
- [122] X. Fu, X. Wang, Y. Yang, B. Chang, Y. Du, J. Zhang, and R. Fu, Optimizing GaN photocathode structure for higher quantum efficiency, *Optik* **123**, 765 (2012).
- [123] X. Fu and J. Zhang, Reactivation of gallium nitride photocathode with cesium in a high vacuum system, *Optik* **124**, 7007 (2013).
- [124] O. H. W. Siegmund, J. S. Hull, A. S. Tremsin, J. B. McPhate, A. M. Dabiran, M. Arnaud, S. S. Murray, and T. Takahashi, Gallium nitride photocathodes for imaging photon counters, *Proc. SPIE* **7732**, 77324T (2010).
- [125] G. V. Benemanskaya, V. N. Zhmerik, M. N. Lapushkin, and S. N. Timoshnev, Charge accumulation nanolayer: A 2D electronic channel in Cs/n-InGaN ultrathin interfaces, *Phys. Solid State* **51**, 395 (2009).
- [126] T. Nishitani, T. Maekawa, M. Tabuchi, T. Meguro, Y. Honda, H. Amano, J. I. Chyi, H. Fujioka, and H. Morkoc, Photocathode electron beam sources using GaN and InGaN with NEA, *Proc. SPIE* **9363**, 93630T (2015).
- [127] J. Qiao, R. Du, H. Ding, Y. Gao, B. Chang, Y. Jiang, J. Yu, and B. Kippelen, Study on photoemission surface of varied doping GaN photocathode, *Proc. SPIE* **9284**, 92840H (2014).
- [128] X.-Q. Fu, B.-K. Chang, X.-H. Wang, B. Li, Y.-J. Du, and J.-J. Zhang, Photoemission of graded-doping GaN photocathode, *Chin. Phys. B* **20**, 037902 (2011).
- [129] S. Xia, L. Liu, and Y. Kong, Research on quantum efficiency and photoemission characteristics of negative-electron-affinity GaN nanowire arrays photocathode, *Opt. Quantum Electron.* **48**, 306 (2016).
- [130] G. Hao, F. Shi, H. Cheng, B. Ren, and B. Chang, Photoemission performance of thin graded structure AlGaIn photocathode, *Appl. Opt.* **54**, 2572 (2015).
- [131] N. Miller, R. E. Jones, K. M. Yu, J. W. Ager, Z. Liliental-Weber, E. E. Haller, W. Walukiewicz, T. L. Williamson, M. A. Hoffbauer, T. Palacios, and D. Jena, Low-temperature grown compositionally graded InGaIn films, *Phys. Status Solidi C* **5**, 1866 (2008).
- [132] T. L. Williamson, J. J. Williams, J. C. D. Hubbard, and M. A. Hoffbauer, High In content In_xGa_(1-x)N grown by energetic neutral atom beam lithography and epitaxy under slightly N-rich conditions, *J. Vac. Sci. Technol. B* **29**, 03C132 (2011).
- [133] M. A. Hoffbauer, T. L. Williamson, J. J. Williams, J. L. Fordham, K. M. Yu, W. Walukiewicz, and L. A. Reichertz, In-rich InGaIn thin films: Progress on growth, compositional uniformity, and doping for device applications, *J. Vac. Sci. Technol. B* **31**, 03C114 (2013).
- [134] These facilities, and the recently commissioned Applied Cathode Enhancement and Robustness Technology (ACERT) photocathode facility, are described at www.lanl.gov/acert.
- [135] W. Walukiewicz, J. W. Ager, K. M. Yu, Z. Liliental-Weber, J. Wu, S. X. Li, R. E. Jones, and J. D. Denlinger, Structure and electronic properties of InN and In-rich group III-nitride alloys, *J. Phys. D* **39**, R83 (2006).
- [136] R. F. Service, Nitrides race beyond the light, *Science* **327**, 1598 (2010).
- [137] A. H. Mueller, E. A. Akhador, and M. A. Hoffbauer, Low-temperature growth of crystalline GaN films using energetic neutral atomic-beam lithography/epitaxy, *Appl. Phys. Lett.* **88**, 041907 (2006).
- [138] A. H. Mueller, M. A. Petruska, M. Achermann, D. J. Werder, E. A. Akhador, D. D. Koleske, M. A. Hoffbauer, and V. I. Klimov, Multicolor light-emitting diodes based on semiconductor nanocrystals encapsulated in GaN charge injection layers, *Nano Lett.* **5**, 1039 (2005).
- [139] W. Lee, J. Limb, J. H. Ryou, D. Yoo, M. A. Ewing, Y. Korenblit, and R. D. Dupuis, Nitride-based green light-emitting diodes with various p-type layers, *J. Disp. Technol.* **3**, 126 (2007).
- [140] Y.-H. Cho, Y. P. Sun, H. M. Kim, T. W. Kang, E.-K. Suh, H. J. Lee, R. J. Choi, and Y. B. Hahn, High quantum efficiency of violet-blue to green light emission in InGaIn quantum well structures grown by graded-indium-content profiling method, *Appl. Phys. Lett.* **90**, 011912 (2007).
- [141] D. J. Leopold, J. H. Buckley, and P. Rebillot, High quantum efficiency ultraviolet/blue AlGaIn-InGaIn photocathodes grown by molecular-beam epitaxy, *J. Appl. Phys.* **98**, 043525 (2005).
- [142] M. Ruiz-Osés, S. Schubert, K. Attenkofer, I. Ben-Zvi, X. Liang, E. Muller, H. Padmore, T. Rao, T. Vecchione, J. Wong, J. Xie, and J. Smedley, Direct observation of bi-alkali antimonide photocathodes growth via in operando x-ray diffraction studies, *APL Mater.* **2**, 121101 (2014).
- [143] S. Shubert, J. Wong, J. Feng, S. Karkare, H. Padmore, M. Ruiz-Osés, J. Smedley, E. Muller, Z. Ding, M. Gaowei, K. Attenkofer, X. Liang, J. Xie, and J. Kühn, Bi-alkali antimonide photocathode growth: An x-ray diffraction study, *J. Appl. Phys.* **120**, 035303 (2016).
- [144] J. Feng, J. Nasiatka, W. Wan, T. Vecchione, and H. A. Padmore, A novel system for measurement of the transverse electron momentum distribution from photocathodes, *Rev. Sci. Instrum.* **86**, 015103 (2015).
- [145] R. Stratton, Theory of field emission from semiconductors, *Phys. Rev.* **125**, 67 (1962).
- [146] J. M. Maxson, I. V. Bazarov, W. Wan, H. A. Padmore, and C. E. Coleman-Smith, Fundamental photoemission brightness limit from disorder induced heating, *New J. Phys.* **15**, 103024 (2013).